

1 **Revision 1**

2 **Quantifying the proportions of relict igneous and metamorphic minerals in orthogneiss:**  
3 **linking metamorphic efficiency to deformation**

4 Timothy Chapman<sup>1\*</sup>, Geoffrey L. Clarke<sup>1</sup>, Sandra Piazzolo<sup>2+</sup> and Nathan R. Daczko<sup>2</sup>.

5 <sup>1</sup>School of Geosciences, The University of Sydney, NSW, 2006, Australia

6 <sup>2</sup>ARC Centre of Excellence for Core to Crust Fluid Systems and GEMOC, Department of  
7 Earth and Planetary Sciences, Macquarie University, NSW, 2109, Australia

8 <sup>+</sup> Current address: School of Earth and Environment, University of Leeds, United Kingdom

9 \*Corresponding author: [t.chapman@sydney.edu.au](mailto:t.chapman@sydney.edu.au)

10 **ABSTRACT**

11 A novel method utilising crystallographic orientation and mineral chemistry data, based on  
12 large-scale electron back-scatter diffraction (EBSD) and microbeam analysis, quantifies the  
13 proportion of relict igneous and neoblastic minerals forming variably deformed high-grade  
14 orthogneiss. The Cretaceous orthogneiss from Fiordland, New Zealand, comprises  
15 intermediate omphacite granulite interlayered with basic eclogite, which were  
16 metamorphosed and deformed at  $T \approx 850^\circ\text{C}$  and  $P \approx 1.8$  GPa after protolith cooling. Detailed  
17 mapping of microstructural and physiochemical relations in two strain profiles through subtly  
18 distinct intermediate protoliths indicates that up to 32% of the orthogneiss mineralogy is  
19 igneous, with the remainder being metamorphic. Domains dominated by igneous minerals  
20 occur preferentially in strain shadows to eclogite pods. Distinct metamorphic stages can be  
21 identified by texture and chemistry, and were at least partially controlled by strain magnitude.  
22 At the grain-scale, the coupling of metamorphism and crystal plastic deformation appears to  
23 have permitted efficient transformation of an originally igneous assemblage. The effective  
24 distinction between igneous *and* metamorphic paragenesis and their links to deformation

25 history enables greater clarity in interpretations of the make-up of the crust and their causal  
26 influence on lithospheric scale processes.

27 **Keywords:** neoblasts, EBSD, recrystallization, strain, tectonometamorphism, microstructure

## 28 INTRODUCTION

29 It is generally considered that elevated temperature conditions in Earth's crust (e.g. >750°C)  
30 are accompanied by widespread metamorphic equilibration, on account of elemental  
31 diffusion distances being comparable to, or larger than the grain-scale (Powell et al., 2005).  
32 Typically, metamorphic transformation is aided by pervasive deformation and the abundance  
33 of fluid (H<sub>2</sub>O or melt: Štípská & Powell, 2005; Powell et al., 2005). However, the persistence  
34 of high proportions of metastable minerals in orthogneiss exhumed from the lower crust is  
35 common (e.g. Austrheim et al., 1997, Štípská & Powell, 2005; Racek et al., 2008). In  
36 circumstances involving inhibited metamorphism, parts of a given rock can be incompletely  
37 equilibrated (Vernon et al., 2008, 2012). The efficiency and scale of metamorphic  
38 equilibration must be queried in the context of results from analogue experiments and mineral  
39 equilibria modelling to provide a robust understanding of the inferred petrogenesis (Powell et  
40 al., 2005; Štípská & Powell, 2005). In turn, mineral chemistry and texture can be used to  
41 recover dynamic changes in extrinsic conditions that can be extrapolated to make  
42 geodynamic inferences (Marmo et al., 2002; Chapman et al., 2017).

43 In circumstances of inefficient metamorphism, sites of mineral reaction can be highly  
44 localised (e.g. Austrheim et al., 1997; Jamtveit et al., 2000) and can contribute to the  
45 partitioning of strain during deformation (Williams et al., 2014). A dynamic feedback  
46 between reaction kinetics and recrystallization mechanisms can accentuate reaction  
47 localisation and mechanical differentiation (Yund & Tullis, 1991; Stünitz, 1998; Piazzolo et  
48 al., 2016). Most studies of inhibited metamorphism focus on linking mineralogical change to  
49 brittle failure and/or fluid ingress (e.g. Jamtveit et al., 2000); there are few studies that assess

50 the role of dynamic recrystallization during ductile deformation (e.g. Svahnberg & Piazzolo,  
51 2010; Satsukawa et al., 2015). Changes in mineralogy have a direct bearing on the rheology  
52 and density of the lithosphere (Jackson et al., 2004; Bürgmann & Dresen, 2008; Chapman et  
53 al., 2017). It is commonly assumed in the application of geodynamic models that  
54 metamorphism in the lower crust is highly efficient, yet this is an over simplification.  
55 Inefficient metamorphism is commonly associated with low heat- and/or fluid-flux  
56 environments, as occurs in cratons, but can also occur in orogenic settings due to changes in  
57 key extrinsic variables (Štípská & Powell, 2005; Racek et al., 2008; Daczko et al., 2009).  
58 There is a need to establish a method to calculate the proportions of igneous material in  
59 partially metamorphosed and deformed granitoids from such settings.

60 In this paper, we quantify the proportions of igneous and metamorphic minerals in a  
61 case study of rocks that show partial to complete metamorphic transformation at high-*T* and  
62 high-*P* conditions ( $T \approx 850^\circ\text{C}$  and  $P \approx 1.8$  GPa). We use unique exposures of rocks exhumed  
63 from lower crustal conditions in Fiordland, New Zealand, that preserve composite layered  
64 plutons, patchily deformed and transformed to granulite and eclogite (De Paoli et al., 2009,  
65 2012). Metamorphism and deformation occurred immediately after, and plausibly  
66 concurrently with, the high-pressure emplacement of the plutons, but was spatially restricted.  
67 This example conflicts with most of the generalisations of lower crust behaviour through: (1)  
68 preserving igneous minerals and textures that metastably persisted at high-*T* conditions;  
69 largely because of (2) strain localization. A method to quantify the proportions of igneous  
70 relicts and the degree of metamorphic growth is established using mineral structural timing  
71 relationships, quantitative crystallographic orientation analysis coupled with mineral  
72 chemistry. Mineralogy outlined by the technique includes: (1) phenocrystal relicts, that have  
73 distinctive orientation and highly distributed lattice strain; (2) neoblastic grains associated  
74 with deformation structures that can be distinguished from igneous reactants by chemistry,

75 crystallographic orientation characteristics and grain size; and (3) partially modified igneous  
76 grains, that underwent chemical change in localised (micron to mm-scale) regions associated  
77 with deformation structure. The primary focus of this study is to distinguish neoblasts from  
78 igneous (protolith) material. It is shown that, despite *PT* conditions considered amenable to  
79 metamorphic conversion and crystal plastic deformation, metamorphic transformation and  
80 neocrystallization was inhibited in up to 32% of the rock volume.

## 81 **THE BREAKSEA ORTHOGNEISS**

82 The Fiordland region on the South Island of New Zealand preserves a disrupted section of the  
83 Late Cretaceous palaeo-Pacific Gondwanan margin. Mafic to intermediate rocks of the  
84 Western Fiordland Orthogneiss (WFO) are parts of a larger Cretaceous arc batholith (*c.* 125–  
85 111 Ma: Bradshaw, 1989; Allibone et al., 2009; Milan et al., 2016, 2017). The Breaksea  
86 Orthogneiss is the highest-pressure unit in the WFO (Fig. 1a), preserving omphacite granulite  
87 and eclogite ( $T \approx 850^\circ\text{C}$  and  $P \approx 1.8$  GPa: De Paoli et al., 2009). It is composite, being  
88 formed mostly of monzodioritic to monzogabbroic omphacite granulite (*c.* 60–65%), cognate  
89 monzodioritic omphacite–orthopyroxene granulite (*c.* 5–10%), and cumulate basite (now  
90 eclogite; *c.* 25%), clinopyroxenite and garnetite (*c.* 5%) (De Paoli et al., 2009; Clarke et al.,  
91 2013; Chapman et al., 2015).

92 This layered protolith is inferred to have been emplaced at high-*P* conditions (1.8–2.0  
93 GPa) between *c.* 124 and 115 Ma (Milan et al., 2016; Stowell et al., 2017). It was  
94 incompletely metamorphosed and deformed ( $D_1$ ) during cooling, initially at the emplacement  
95 depth (Table 1: Chapman et al., 2017). The presence of mutually cross-cutting igneous veins  
96 and  $S_1$  folia are consistent with the  $D_1$  event having occurred late in the protolith  
97 crystallization. The  $S_1$  foliation commonly includes steep S-L fabrics that transpose planar  
98 igneous layering (Chapman et al., 2017) and is deformed into metre to km-scale concentric  
99 domes (Betka & Klepeis, 2013). Post- $S_1$  decompression to lower grade conditions ( $P \approx 1.0$ –

100 1.4 GPa and  $T \approx 650\text{--}750^\circ\text{C}$ ) is recorded by diopside and albite symplectite that  
101 pseudomorph  $S_1$  omphacite (De Paoli et al., 2009) and corresponds to a period of extensional  
102 dome formation (Klepeis et al., 2016; Chapman et al., 2017). Localized  $D_2$  amphibolite facies  
103 shear zones cut igneous layering and  $S_1$  folia, and are thought to have formed during orogenic  
104 collapse possibly coupled with root foundering (Fig. 1a; Klepeis et al., 2007; Chapman et al.,  
105 2017).

106 The spectrum of whole-rock compositions in the main rock types of the Breaksea  
107 Orthogneiss define linear first-order trends in Harker plots from peridotgabbro to  
108 monzodiorite (De Paoli et al., 2009, 2012). These compositional variations are mostly  
109 attributed to cumulate processes and magma redox conditions that preceded high-grade  
110 deformation (Clarke et al., 2013; Chapman et al., 2015; Cyprych et al., 2017). Interlayered  
111 near-monomineralic garnetite and clinopyroxenite retain delicate cumulate microstructure  
112 and unique crystallographic fabrics (Fig. S1: Clarke et al., 2013; Cyprych et al., 2017).  
113 Igneous clinopyroxene and garnet are well preserved in these ultra-basic cumulate layers;  
114 they have rare earth element (REE) chemistry that overlap with that of clinopyroxene and  
115 garnet in basic and intermediate protoliths (Clarke et al., 2013). A commonality in mineral  
116 REE chemistry coupled with the preservation of igneous microstructure supports the  
117 interpretation of the basic and ultrabasic components being cumulates of basic to  
118 intermediate magmatism (Fig. S1: Clarke et al., 2013).

119 Mineral chemical relationships identified in ultrabasic components of the Breaksea  
120 Orthogneiss can be partially extended into its felsic components. However, metamorphism  
121 was more pervasive in felsic portions of the orthogneiss, presumably because of rheological  
122 distinctions (Chapman et al., 2015; Miranda & Klepeis, 2016). Igneous and metamorphic  
123 (neoblastic) garnet can be distinguished by the following textural and chemical features (after  
124 Clarke et al., 2013). Large igneous garnet and omphacite occur as euhedral grains in cm-scale

125 clusters, with garnet heavy-REE-enriched patterns overlapping with those of igneous garnet  
126 in eclogite and garnetite. Garnet phenocrysts also have rutile exsolution and lack positive Eu  
127 anomalies, consistent with their growth from a high-*T* liquid (>1000°C: Chapman et al.,  
128 2017) and inconsistent with peritectic growth from prograde incongruent partial melting  
129 (Clarke et al., 2013). Idioblastic metamorphic garnet is commonly symplectic with quartz,  
130 forms coronae to omphacite and plagioclase, is heavy-REE depleted and has a positive Eu  
131 anomaly. Other rock-forming minerals have relationships that are ambiguous, but are likely  
132 to have involved a combination of igneous and metamorphic histories dependent on strain  
133 intensity. Foliated assemblages of omphacite, garnet, plagioclase, kyanite and rutile are  
134 consistent with metamorphism at conditions of the omphacite granulite sub-facies (De Paoli  
135 et al., 2012; Clarke et al., 2013). Other portions of the felsic rocks, typically in low-strain  
136 domains, have igneous grain shapes with compositions that are consistent with a parental  
137 magma crystallising Ca–Na clinopyroxene with or without garnet or orthopyroxene  
138 (Chapman et al., 2015). The extent of neocrystallization in the felsic lower crustal rocks is the  
139 focus of this study.

#### 140 **Field Relationships**

141 The primary igneous fabric at Breaksea Tops involves both gradational and sharp contacts  
142 between distinct layers in the intermediate rocks and the decimetre-scale cumulate pods, that  
143 are defined by variations in the proportions of garnet, clinopyroxene, orthopyroxene and  
144 plagioclase. The layering is locally transposed into a moderately dipping (>65°), north-west-  
145 striking gneissic foliation ( $S_1$ ) with an associated  $L_1$  mineral stretching lineation plunging  
146 towards the southeast (Fig. 1a). The gneissic fabric is defined by elongate and aligned cm-  
147 scale garnet–pyroxene grain clusters in intermediate gneiss (“mafic clusters”). Deformation  
148 of  $S_1$  folia into concentric domes is not observed at the Breaksea Tops and appear to be  
149 spatially related to the extensional  $D_2$  Resolution Island Shear Zone (RISZ) in Breaksea

150 Sound (Fig. 1a: Betka & Klepeis, 2013; Klepeis et al., 2016). At Breaksea Tops,  $S_1$  folia are  
151 deflected around competent basite pods, with the intensity of the lineation increasing away  
152 from the pods (Fig. 1b). Decimetre- to decametre-scale low-strain domains commonly occur  
153 in strain shadows of the basic components (Fig. 1b), where igneous layering that lacks a  
154 penetrative mineral lineation is cut by  $S_1$ .

155 Fifteen orientated samples were collected from the layered parts of the  
156 monzogabbroic to monzodioritic gneiss from a ridge transect at the Breaksea Tops (Fig. 1a).  
157 The sample suite includes a transition from rocks with shallowly-dipping igneous layering, to  
158 those with well-developed moderately-dipping  $S_1$ - $L_1$  fabrics (Fig. 2a). The distinction of  
159 magmatic and tectonic fabrics, and in particular the aspect ratio of minerals defining  $L_1$ , was  
160 used to assess strain (Fig. 2b; Flinn, 1965). Modal layering resulted in the preservation of two  
161 strain series across subtly distinct protoliths: (1) a monzogabbro that records low to  
162 intermediate strain; and (2) a monzodiorite that records intermediate to high strain. Detailed  
163 mapping of the samples was used to determine the area percentage of each protolith and  
164 strain type across the Breaksea Top transect (Fig. 2b). Approximately 27% of the outcrop  
165 involved monzogabbroic gneiss that records largely low strain magnitude. It transitions into  
166 intermediate  $L_1$ - $S_1$  fabrics in ~ 40% of the outcrop area. High-strain monzodioritic gneiss,  
167 marked by linear ( $L_1 > S_1$ ) fabrics and coronitic garnet development, covers ~ 20% of the  
168 outcrop area. Protoliths to these zones are preserved as intermediate strain layers in only 13%  
169 of the outcrop. A series of four samples were selected for detailed petrographic and  
170 microstructural investigation (Fig. 2a).

## 171 METHODS

172 Optical petrographic and microstructural observations were coupled with focused (areas of *c.*  
173 2 x 2 mm) and large-scale (areas of 1 x 1.5 cm) quantitative crystallographic orientation  
174 mapping using the electron back-scatter diffraction (EBSD) technique (Prior et al. 1999).

175 Mineral chemical analysis was undertaken on the same samples and within the region of  
176 EBSD mapping. All thin sections were prepared perpendicular to the foliation (XY plane)  
177 and parallel to the lineation (Z direction). Aspect ratios ( $AR = \text{long/short axes}$ ) of mafic grain  
178 clusters on planes parallel to the lineation (XZ plane) were used to quantify strain intensity  
179 together with  $D = \sqrt{[\ln(X/Y)^2 + \ln(Y/Z)^2]}$  (Fig. 2b) following Flinn (1965).

#### 180 **Quantitative crystallographic orientation analysis**

181 Electron back-scatter diffraction (EBSD) investigation was performed using a Zeiss EVO Ma  
182 15 scanning electron microscope (SEM) housed at Macquarie Geoanalytical at Macquarie  
183 University, Sydney. Additional data was also collected on a Zeiss Ultra Plus SEM at the  
184 Australian Centre for Microscopy and Microanalysis (ACMM) at the University of Sydney.  
185 Etched polished thick sections (*c.* 100  $\mu\text{m}$ ) were analysed at an accelerating voltage of 20–  
186 30 kV, with a beam current of 8 nA and a working distance of  $\sim$ 9–14 mm. Electron  
187 backscatter diffraction patterns were automatically acquired and indexed using Oxford  
188 Instruments AzTEC software (<https://www.oxford-instruments.com/>). The EBSD patterns  
189 were collected in regular grids where the sampling step size varied from 2 to 8  $\mu\text{m}$  for  
190 detailed microstructural areas and 15 to 18  $\mu\text{m}$  for whole thin-section mapping. For each data  
191 point the crystallographic orientation of the mineral was determined based on Kikuchi  
192 diffraction patterns (Prior et al., 1999). Post-processing was undertaken in the Channel 5  
193 TANGO software (Oxford Instruments) following procedures described by Prior et al. (2002)  
194 and Piazzolo et al. (2006). The post-processing methods are designed to remove false data  
195 (misidentified during scanning) and to enhance data continuity over the microstructures in  
196 relation to the overall scan index rate. Modal abundances were determined using volume  
197 calculations on thin-section scale EBSD maps in Channel 5 (Table 2). The calculations were  
198 compared to mineral equilibria modelling results of Chapman et al. (2017) to assess the  
199 potential extent of equilibration.



200 In the following analysis, grains are defined as areas enclosed by boundaries of  
201 greater than  $10^\circ$  of misorientation, referring to the distortion of the crystalline lattice;  
202 boundaries with misorientations less than  $10^\circ$  but greater than  $2^\circ$  are referred to as low-angle  
203 boundaries. If the low-angle boundaries have crystallographic rotational characteristics and  
204 lattice distortions consistent with recovery they are defined as subgrain boundaries (sgb).  
205 Grain internal strain was estimated following Piazzolo et al. (2006), where a grain with an  
206 average internal misorientation of  $<1^\circ$  is denoted as substructure-free.

207 We utilize the strength of the crystallographic preferred orientation (CPO) as an  
208 additional measure of strain intensity. This has been evaluated by calculating the texture  
209 index ( $J$ : after Bunge, 1982) in the MTEX software package (Mainprice et al. 2011) for  
210 omphacite and plagioclase. The texture index has a value of one for a random distribution  
211 and an infinite value for a single crystal (Bunge, 1982).

## 212 **Mineral chemistry**

213 Mineral chemical data for the studied samples and specific microstructures presented here  
214 (Table 3) complements detail mineral chemical relationships already published on the  
215 Breaksea Orthogneiss (De Paoli et al., 2009; Clarke et al., 2013; Chapman et al., 2015). The  
216 major element content of the rock-forming minerals was determined using the same polished  
217 thin/thick sections as those for EBSD and a CAMEBAX SX100 electron microprobe (EMP)  
218 housed at Macquarie Geoanalytical. Operating conditions for the EMP involved 15 kV  
219 accelerating voltage and a beam current of 20 nA. Energy-dispersive spectrometry X-ray  
220 maps collected simultaneously during EBSD acquisition on the Zeiss SEMs housed at both  
221 Macquarie Geoanalytical and ACMM provided additional information on spatially resolved  
222 chemical differences for the larger scale microstructural assessment. Garnet stoichiometry  
223 and ferric iron correction was applied after Droop (1987), whereas clinopyroxene end-  
224 member calculations follow Morimoto (1989).

225

## 226 **Timing of mineral growth**

227 We use the timing relationships of mineral growth relative to  $S_1$  crystal-plastic deformation to  
228 distinguish between different crystal growth periods namely pre- $D_1$  igneous, syn-, and post-  
229  $D_1$  metamorphic. To distinguish between igneous relicts and syn-deformational growth we  
230 designated grain as neoblastic if they exhibit (i) low internal misorientation ( $<3^\circ$ ), (ii) a small  
231 grain size ( $<500 \mu\text{m}$ ), (iii) a pronounced crystallographic preferred orientation (CPO) that  
232 matches a collective maximum and (iv) a chemical distinction that matches predicted  
233 metamorphic mineral equilibria (e.g. jadeite-rich omphacite, grossular-rich garnet and albitic  
234 plagioclase) as identified by Chapman et al. (2017). All other grains that do not fit these  
235 criteria are considered to be igneous relicts. The relicts additionally preserve their own  
236 weaker igneous CPO together with igneous microstructures (e.g. Vernon et al., 2012).  
237 Igneous relicts and neoblastic volumes were calculated via the combination of these criteria  
238 from large EBSD combined with the simultaneously acquired EDS maps within the TANGO  
239 software. Diffusive modification of the igneous relicts was not accounted for in the volume  
240 calculations due the delicate scale of these features. In generally, the method biases towards  
241 larger features, as any feature smaller than 2 times the analysis step size cannot be resolved.  
242 However, optical analysis shows that very few features are at this range (cf. Fig. 3).  
243 Furthermore, the slow igneous cooling times of the orthogneiss (c. 8–9 Myr) suggested by U–  
244 Pb zircon and Sm–Nd garnet ages greatly minimises these limitations (e.g. Stowell et al.,  
245 2017). Although, occurrences of late magma injections could partially obscure the structural  
246 relationships (Clarke et al., 2013), thus these areas were purposely avoided during sampling.

247

## **RESULTS**

### 248 **Crystallographic preferred orientations (CPO)**

249 Crystallographic preferred orientations for omphacite and plagioclase are shown in Figures 4  
250 and 5. Omphacite CPO is defined by a  $\langle 001 \rangle$  point maxima contained within the foliation  
251 plane and  $\langle 010 \rangle$  and  $\{110\}$  maximums forming a girdle normal to the foliation (Fig. 4).  
252 Omphacite grains with orientations distinct from this dominant CPO include porphyroclasts,  
253 coarse grain fractions ( $>300 \mu\text{m}$ ), small euhedral grains in the matrix and mineral inclusions  
254 in garnet cores (Fig. 3). The principle axes of these grains do not coincide with the  $D_1$  fabric  
255 trajectories (Fig. 6h), instead matching the CPO preserved in the cumulate layers (Fig. S1).  
256 The strength ( $J$ ) of the CPO increases from 1.62 to 1.81 between low and intermediate-strain  
257 monzogabbroic gneiss, and from 4.10 to 7.17 between intermediate and high-strain  
258 monzodioritic gneiss. The change is consistent with the variation in cluster aspect ratios (Figs  
259 2b & 4). Plagioclase CPO involves a  $\langle 001 \rangle$  point maxima parallel to the lineation and  $\langle 010 \rangle$   
260 axis and (010) poles normal to the foliation (Fig. 5). The plagioclase fabric progressively  
261 strengthens from low- to intermediate-strain monzogabbroic gneiss ( $J = 2.94$  to  $5.74$ ) and  
262 from intermediate to high-strain monzodioritic gneiss ( $3.14$  to  $6.05$ ). Both these CPO are  
263 consistent with large data compilations of the WFO from distinct structural levels (Cyprych  
264 et al., 2017).

### 265 **Microstructures and quantitative orientation analysis**

266 According to the finite strain analysis (Fig. 2) and increasing  $J$ -index of plagioclase and  
267 omphacite (Figs 2–4) we describe the microstructures in the order of increasing strain. Low-  
268 strain samples as those that exhibit an average  $AR$  of  $< 2$  ( $D = 0.45$ – $0.54$ ), intermediate strain  
269 samples show  $2 \leq \text{average } AR \leq 3$  ( $D = 0.74$ – $1.19$ ), while high-strain samples are  
270 characterized by average  $AR > 3$  ( $D = 1.31$ – $1.75$ ) (Fig. 2b & 3).

#### 271 **Low strain: monzogabbroic gneiss (0904D)**

272 Low-strain samples of monzogabbroic gneiss are generally coarse grained ( $400$ – $1000 \mu\text{m}$ )  
273 with equant to elongate mafic grain clusters of garnet and omphacite ( $AR = 1$ – $4$ ). Large

274 omphacite (500–1000  $\mu\text{m}$ ) in most grain clusters has intracrystalline lattice distortions of 5–  
275  $8^\circ$  and is surrounded by smaller neoblasts with serrated grain boundaries and low internal  
276 deformation (Figs 3a, 6a & b). The large omphacite cores have faceted inclusions of  
277 plagioclase (Fig. 3b). Tabular omphacite grain shapes, with straight coincident faces and low  
278 apparent dihedral angles can be present in some clusters and locally intergrown with  
279 plagioclase laths in strain shadows (Fig. 3a). Grain cores of large garnet have rutile  
280 exsolution lamellae and euhedral inclusions of antiperthite feldspar and omphacite (Fig. 3c).  
281 Garnet porphyroclasts are generally substructure free, though low-angle boundaries with up  
282 to  $4^\circ$  of misorientation can be present (Fig. 6a). The distribution of crystallographic  
283 orientations across these garnet boundaries define rotational characteristics consistent with  
284 subgrain arrays (Fig. 6c). The plagioclase-rich matrix away from strain shadows or mafic  
285 cluster margins is generally granoblastic (200–300  $\mu\text{m}$ ) with texturally equilibrated triple  
286 junctions ( $120^\circ$ ) (Fig. 3d). At the margins of mafic clusters plagioclase grain size is  
287 appreciably reduced ( $<150 \mu\text{m}$ ) and core-and-mantle microstructures are more common (Fig.  
288 3d). The plagioclase porphyroclasts ( $>300 \mu\text{m}$ ) exhibit undulose extinction, tapered  
289 deformation twins and irregular or sutured grain boundaries with minor bulging. The primary  
290 grain form is consistent with coincidental dihedral angles being partially overprinted during  
291 recrystallization (Fig. 3d). The porphyroclasts exhibit internal misorientation of up to  $8^\circ$   
292 along the entire diameter of the grain. Surrounding the porphyroclasts are fine ( $<150 \mu\text{m}$ )  
293 plagioclase neoblasts (Fig. 3d).

#### 294 **Intermediate strain: monzogabbroic gneiss (0905B)**

295 Gneissic layering is pronounced in intermediately strained monzogabbroic gneiss (1-3 mm:  
296 Fig. 2a). The attenuated and asymmetric mafic clusters ( $AR = 2-6$ ) distinctively anastomose  
297 around large garnet porphyroclasts ( $>1000 \mu\text{m}$ ) (Figs 2a & 6c). Omphacite porphyroclasts  
298 (400–1000  $\mu\text{m}$ ) in cluster interiors are equant to weakly elongate ( $AR = 2-3$ ). The

299 porphyroclasts display significant intracrystalline lattice distortion ( $6\text{--}15^\circ$ ) and variable  
300 degrees of low-angle boundary development (Figs 6e & f). Smaller omphacite grains form  
301 tails to mafic clusters ( $50\text{--}400\ \mu\text{m}$ ) and generally have less internal lattice distortion ( $<3^\circ$ ),  
302 though some exhibit low-angle boundary arrays (Figs 6e & g). All omphacite grains maintain  
303 close to  $120^\circ$  mutual junctions. Porphyroclastic garnet generally has limited crystal lattice  
304 distortion ranging up to  $3^\circ$  across the grains. Although, some grains have low-angle  
305 boundaries with up to  $\sim 8^\circ$  of distortion. Faceted inclusions of substructure-free omphacite  
306 are present in the garnet cores. Coronate garnet surrounds some mafic clusters. Plagioclase  
307 exhibits less prevalent core-and-mantle microstructures than present in the lower-strain  
308 samples, although when present they occur in the centre of feldspar-rich domains (Fig. 3f).  
309 Plagioclase porphyroclasts ( $200\text{--}600\ \mu\text{m}$ ) exhibit intracrystalline lattice distortion of  $\sim 8^\circ$  and  
310 have developed subgrain regions similar in size to mantled grains ( $50\text{--}150\ \mu\text{m}$ ; Fig. 3f).  
311 Outside of these domains granoblastic habit predominates the feldspar-rich matrix. Highly  
312 deformed omphacite fish (up to  $700\ \mu\text{m}$ ) occur occasionally in the feldspar-rich matrix (Fig.  
313 7).

#### 314 **Intermediate strain: monzodioritic gneiss (1203T)**

315 Asymmetric gneissic layering and stretching is extremely pronounced in intermediate-strain  
316 monzodioritic gneiss ( $AR = 2\text{--}6$ ). Elongate omphacite grain shapes are apparent for large  
317 crystals ( $2500\ \mu\text{m}$ ) that define irregular habits (Figs 3g & 8a). Large tabular omphacite grains  
318 have titanite-hematite exsolution lamellae in grain cores. The omphacite porphyroclasts have  
319 significant internal lattice distortion (up to  $15^\circ$ ), localised along curved low-angle boundaries  
320 ( $>2^\circ$ ; Figs 8b & d). The rotation of the crystallographic axes across the low-angle boundaries  
321 is consistent with them representing subgrain arrays (Fig. 8f). The size of the areas enclosed  
322 by the subgrains boundaries ( $\sim 400\ \mu\text{m}$ ) match the sizes of equant finer grains that form the  
323 flaser tails. The grains forming the tails have low internal misorientation ( $<3^\circ$ ) or are

324 substructure-free (Figs 8c & e). The plagioclase matrix is typically granoblastic with  
325 prevalent equilibrium triple junctions. Large plagioclase grains (>500  $\mu\text{m}$ ) have an  
326 abundance of tapered albite twins, which accommodate most of the lattice distortion ( $3^\circ$ ).  
327 Although, some plagioclase grains have misorientation of up to  $9^\circ$  accommodated along  
328 subgrain boundary arrays. Distinct intergrowths ( $\sim 300 \mu\text{m}$ ) of K-feldspar and plagioclase  
329 occur in the strain shadows and around the margins of elongate grain clusters. The  
330 intergrowths show similarity in the crystallographic orientations between both feldspar  
331 minerals. Plagioclase grains within the intergrowths has deformation focussed on albite twins  
332 whereas K-feldspar has intracrystalline lattice distortions of up to  $5^\circ$ .

### 333 **High strain: monzodioritic gneiss (1203C)**

334 Mafic grain clusters in high-strain monzodioritic gneiss are extremely stretched (*AR* of up to  
335 7). The clusters are enveloped entirely by garnet necklaces intergrown with quartz and rutile  
336 (Fig. 3g). Garnet in these structures has vermicular to tabulate quartz inclusions commonly  
337 aligned sub-parallel to its crystal faces. Omphacite and feldspar are granoblastic and  
338 generally equant, though elongated omphacite can occur in cluster interiors (*AR* of up to 6).  
339 These elongated omphacite grains are large (500–1000  $\mu\text{m}$ ) and surrounded by smaller  
340 equant omphacite grains (100–400  $\mu\text{m}$ ; Fig. 8g). All omphacite has most internal  
341 misorientation ( $9^\circ$ ) completely localised in low-angle boundaries together with triple  
342 junctions approaching  $120^\circ$  (Figs 8g & i). The omphacite grains adjacent to garnet coronae  
343 are free of substructure (Figs 8l & k). The neighbouring garnet grains also generally lack any  
344 substructure. Most of the garnet grains have similar crystallographic orientations and are  
345 separated from adjacent grains by a series of low-angles boundaries ( $2\text{--}5^\circ$ ) (Fig. 8g). All the  
346 grains have crystallographic orientation relationships mimicking neighbouring omphacite  
347 (Fig. 8l). The matrix of the gneiss comprises coarse plagioclase (200–700  $\mu\text{m}$ ) with most  
348 preserving tapered deformation twins (Fig. 3h). The plagioclase grains have well-defined

349 subgrain boundaries, where crystal lattice misorientation (up to 10°) is localised. Minor  
350 proportions of fine-grained plagioclase (100 µm) occur at the triple junctions of the larger  
351 grains. K-feldspar (<125 µm) occurs exclusively in an enveloping texture around garnet  
352 coronae, defining elongated and irregular shapes that are orientated within the foliation plane  
353 (Fig. 8f).

#### 354 **Mineral chemistry**

355 Clinopyroxene is omphacite with jadeite contents ( $Jd =$   
356  $100[(2Na/(2Na+Ca+Mg+Fe^{2+}))(Al_{M1}/(Al_{M1}+Fe^{3+}_{M1}))]$ ) varying throughout the felsic portions  
357 of the orthogneiss. Omphacite grain cores in low-strain monzogabbroic gneiss have lower  
358 jadeite content ( $Jd_{26-27}$ ) than rims or neoblasts ( $Jd_{30-31}$ ) (Fig. 7). An equivalent, though  
359 slightly more pronounced microstructural variation in jadeite content is present in  
360 intermediate-strain monzogabbroic and monzodioritic gneisses with lower absolute values;  
361 porphyroclasts have core to rim zoning of  $Jd_{17-24}$ , whereas grains in cluster tails are  $Jd_{24-33}$ .  
362 (Fig. 9). Omphacite in high-strain samples has a tight compositional range of  $Jd_{24-28}$  (Fig. S2).

363 Garnet end-member proportions were calculated as follows:  $Alm =$   
364  $100Fe^{2+}/(Fe^{2+}+Mn+Mg+Ca)$ ,  $Pyp = 100Mg/(Fe^{2+}+Mn+Mg+Ca)$ ,  $Grs =$   
365  $100Ca/(Fe^{2+}+Mn+Mg+Ca)$  and  $Sps = 100Mn/(Fe^{2+}+Mn+Mg+Ca)$ . Garnet cores in  
366 monzogabbroic gneiss have the lowest grossular and highest pyrope content ( $Alm_{38-39}Pyp_{42-}$   
367  $43Grs_{6-8}Sps_{1-2}$ ), enclosed by comparatively grossular enriched rims ( $Alm_{38-39}Pyp_{37-40}Grs_{8-}$   
368  $13Sps_{1-2}$ ; Fig. 9). Garnet in intermediate-strain monzodioritic gneiss has core compositions of  
369  $Alm_{42-44}Pyp_{35-38}Grs_{12-14}Sps_{1-2}$  zoning to rims that are richer in grossular ( $Grs_{18-25}$ ) but with  
370 lower pyrope ( $Pyp_{30-35}$ ) content (Fig. 9). Garnet compositions in high-strain monzodioritic  
371 gneiss broadly match that of garnet rims in intermediate-strain samples ( $Alm_{37-44}Pyp_{31-}$   
372  $38Grs_{12-18}Sps_{1-2}$ ; Fig. 9).

373 End-member proportions of feldspars were calculated as follows:  $An =$   
374  $100Ca/(Ca+Na+K)$ ,  $Ab = 100Na/(Ca+Na+K)$  and  $Or = 100K/(Ca+Na+K)$ . The cores of large  
375 plagioclase porphyroclasts in monzogabbroic gneiss are comparatively enriched in anorthite  
376 ( $An_{34-35}Ab_{63-64}Or_{1-2}$ ) and enclosed by less anorthitic rims ( $An_{18-22}Ab_{78-79}Or_1$ ; Fig. 9). Core  
377 compositions of plagioclase from intermediate-strain monzogabbroic gneiss are less  
378 anorthitic ( $An_{26}Ab_{73}Or_1$ ) than rims ( $An_{24-27}Ab_{71-73}Or_{1-3}$ ; Fig. 9). Similar plagioclase core–rim  
379 relationship occurs in intermediate-strain monzodioritic gneiss (core:  $An_{28}Ab_{70}Or_2$  and rim:  
380  $An_{20-25}Ab_{73-77}Or_{1-3}$ ; Fig. 9). Plagioclase grain cores in high-strain monzodioritic gneiss have  
381 compositions ( $An_{23-25}$ ) that match those of rims from intermediate-strain monzodioritic  
382 gneiss, whilst rims are more albitic ( $An_{18-24}Ab_{76-79}Or_{1-3}$ ). Orthoclase ( $An_{10-12}Ab_{1-3}Or_{87-88}$ )  
383 occurs intergrown with albitic plagioclase ( $An_{20}Ab_{80}$ ; Fig. 9).

#### 384 **DISCUSSION**

385 The lower continental crust is commonly envisaged to be pervasively deformed (Bürgmann  
386 & Dresen, 2008), but features in many exposed sections are consistent with grossly  
387 heterogeneous strain (Austrheim et al., 1997; White & Clarke, 1997). In such examples,  
388 strong links can be established between regions of deformation and enhanced metamorphic  
389 transformation (Austrheim et al., 1997; White & Clarke, 1997; Jamtveit et al., 2000;  
390 Williams et al., 2014; Satsukawa et al., 2015). The Breaksea Orthogneiss is one such  
391 instance, where variations in plane-strain magnitude are strongly coupled with the extent of  
392 high-*P* Cretaceous metamorphism (Figs 1b & 2b; Clarke et al., 2013; Chapman et al., 2015,  
393 2017). Detailed mineral chemical studies have distinguished igneous from metamorphic  
394 garnet in the orthogneiss and correlated their broad distribution in relation to strain (Clarke et  
395 al., 2013). A similar spatial distribution is apparent for the other rock-forming minerals: there  
396 is a strong association between recrystallization and metamorphic equilibration. This  
397 coincidence presents the opportunity to quantify the proportions of igneous and neoblastic



398 materials (summarised in Fig. 10). Causal links established in two-dimensions at the grain-  
399 scale can be extended to the rock volume and the outcrop-scale based on field mapping (Figs  
400 1–2). These data reveal the efficiency of metamorphism and its links to crystal plastic  
401 deformation that seems common in lower crustal rocks.

#### 402 **Quantifying igneous vs. metamorphic growth: a tool to assess metamorphic efficiency**

403 Rock microstructure can include features that distinguish periods of mineral growth in  
404 addition to the effects of external stress. In a simple sense, differences should be observable  
405 between minerals that have largely crystallized from a silicate liquid (igneous) and those  
406 related to growth in the solid-state (metamorphic) (Vernon et al., 2012; Holness et al., 2018).  
407 Some relevant igneous microstructural features include (after Vernon et al., 2012): euhedral  
408 crystal form, faceted inclusions and dihedral angles consistent with mutual impingement  
409 (Paterson et al., 1989; Holness et al., 2006, 2018). Typically, these features are overprinted  
410 during microstructural maturation (recovery) as a consequence of prolonged heating or  
411 progressive deformation (e.g. Vernon et al., 2012; Holness et al., 2018). However, the effects  
412 of strain partitioning can leave areas that partially preserve igneous microstructure in  
413 mechanically strong grains such as pyroxene or garnet, including faceted euhedral inclusions,  
414 low apparent dihedral angles and delicate exsolution textures (Chapman et al., 2015). The  
415 additional use of crystal orientation data, lattice distortion and mineral chemistry expands the  
416 criteria that can be used to quantify the proportions of igneous *versus* metamorphic minerals.

417 Plastic strain in the Breaksea Orthogneiss during D<sub>1</sub> resulted in a well defined  
418 crystallographic fabric that developed concurrently with a general reduction in grain size (e.g.  
419 Urai et al., 1986; Yund & Tullis, 1991; Stünitz 1998). The effects of heterogenous  
420 deformation are most pronounced in domains that experienced low-strain intensity, leaving  
421 mm to cm gradations in the recrystallization of igneous grains and inefficient recovery (e.g.  
422 Svahnberg & Piazzolo, 2010). Porphyroclasts of omphacite and plagioclase in low-strain

423 domians have appreciable, but patchy, areas with lattice distortion (3–20°) that are spatially  
424 related to the development of a series of low-angle boundaries (2–10°: Figs 6i & 8d) or  
425 deformation twins (Fig. 3). Mechanically strong garnet has comparatively limited lattice  
426 distortion, and grain areas with low-angle boundary development occur where there is higher  
427 strain. Other parts of the orthogneiss that experienced higher strain have attenuated  
428 omphacite clusters and smaller grain sizes (Figs 6 & 8); the effects D<sub>1</sub> strain were more  
429 pervasive. In these instances, metamorphic garnet is mostly interpreted to have  
430 heterogeneously nucleated on phenocrystal clusters of garnet and omphacite, resulting in  
431 prominent necklace microstructures (Figs 6 & 8).

432         Microstructure in the Breaksea Orthogneiss preserves an S<sub>1</sub> CPO that developed  
433 during high-*P* cooling, imposed on an earlier CPO developed during crystallization of the  
434 protolith (Fig. S1; Cyprych et al., 2017). The high-*T* conditions (~850°C) inferred to have  
435 accompanied D<sub>1</sub> deformation and the persistence of abundant lattice distortion (Figs 6a, h &  
436 8f) texture in garnet, pyroxene and plagioclase support an interpretation that S<sub>1</sub> developed via  
437 dislocation creep (after Prior et al., 2002; Brenker et al., 2002; Kruse et al., 2001). Neoblastic  
438 grains in low- and high-strain samples are crystallographically aligned with S<sub>1</sub>. The  
439 orientation of neoblastic omphacite and plagioclase is consistent with active creep along  
440 common slip systems: {110}[001] and (100)[001] in omphacite (after Brenker et al., 2002),  
441 and (010)[001] in plagioclase (after Kruse et al., 2001). Although less distinct, the  
442 crystallographic alignment of garnet neoblasts is controlled by epitaxial growth on omphacite  
443 ( $\{110\}_{\text{Grt}} \parallel \langle 001 \rangle_{\text{Omp}}$ : Fig. 8l). Any deviation from the dominant S<sub>1</sub> CPO is thus considered to  
444 be part of an earlier igneous fabric (Figs 3, 6d & h), marked by coarse-grained  
445 porphyroclastic material (Fig 10).

446         The interpretation of igneous and neoblastic microstructures requires validation  
447 through the characterisation of mineral mode and chemistry, through mineral equilibria

448 modelling (Table 2: after De Paoli et al., 2012; Chapman et al., 2017). The high-variance  
449 breakdown and removal of plagioclase to form omphacite-bearing assemblages in the  
450 Breaksea Orthogneiss is a consequence of the high- $P$  cooling (Green & Ringwood, 1967; De  
451 Paoli et al., 2012; Chapman et al., 2017). Pervasively recrystallised domains have low modes  
452 of comparatively albitic plagioclase, jadeite-rich omphacite, K-feldspar, kyanite and  
453 grossular-rich garnet. The mineral assemblages correspond to  $T = 850^{\circ}\text{C}$  and  $P = 1.8$  GPa  
454 (Fig. 9: Chapman et al., 2017). Parts of the Orthogneiss that experienced low  $D_1$  strain have  
455 appreciably higher modes of more calcic plagioclase (~50%) than is predicted by the  
456 equilibria modelling for the inferred peak conditions (~30%, Table 2; De Paoli et al., 2012;  
457 Chapman et al., 2017). The higher mode of calcic plagioclase is consistent with that predicted  
458 for the crystallisation of a dry monzodioritic liquid at 2.0 GPa (~50%: Clarke et al., 2013). In  
459 addition, porphyroclastic omphacite and garnet have chemical compositions distinct to that  
460 the metamorphic neoblasts grown during recrystallization; the former closely match the  
461 predicted phenocryst compositions (Figs 9 & 10: Clarke et al., 2013).

462         The combination of these petrologic criteria enable the prediction that igneous grains  
463 account for between 60 and 29% of the volume in low to intermediate-strain monzogabbroic  
464 and monzodioritic gneiss, with the remainder being neoblasts (Fig. 11). Highly strained  
465 samples comprise completely neoblastic mineral assemblages. Placing these variations in the  
466 context of observed field strain intensities (Fig. 2b) indicates that 32% of the felsic  
467 proportions Breaksea Orthogneiss can be considered to comprise igneous material. Some of  
468 this was partially modified by changes in the chemical composition of the minerals due to the  
469 effects of the high- $P$  metamorphism. Heterogeneous strain conditions largely accounted for  
470 the conversion of the remainder to omphacite granulite.

471 **Implications: Metamorphic efficiency in the lithosphere**

472 A knowledge of phase stability at distinct  $P$  and  $T$  conditions provides the basis to extrapolate  
473 experimental results and predict lithospheric behaviour (Powell et al., 2005; Bürgmann &  
474 Dresen, 2008). In examples such as the Breaksea Orthogneiss, the efficiency of  
475 metamorphism inherently controlled the proportions of mechanical strong and weak material,  
476 and it can thus result in substantial changes to lower crustal rheology (e.g. Austrheim et al.,  
477 1997; Jackson et al., 2004; Bürgmann & Dresen, 2008). The preservation of large proportions  
478 of phenocrystal material (32% in this case study) in lower crustal rocks reflects strain  
479 partitioning at the microscopic to macroscopic scales (e.g. Williams et al., 2014). This one-  
480 third extent of metastable persistence was common, and plausibly higher, throughout much  
481 the Cretaceous Gondwana margin now exposed in Fiordland (Bradshaw et al., 1989; Daczko  
482 & Halpin, 2009; Chapman et al., 2016). It is also common in other exposures of lower crustal  
483 material (Austrheim et al., 1997; White & Clarke, 1997). It seems reasonable to assume that  
484 the effects of incomplete metamorphism are likely to be more prevalent than commonly  
485 considered for circumstances of patchy deformation, fluid-poor and short-lived metamorphic  
486 events (~10 Myr: Austrheim et al., 1997; Jamtveit et al., 2000; Štípská & Powell, 2005;  
487 Racek et al., 2008).

488 Quantifying the volume proportions of metastably persisting phases is therefore of  
489 practical importance in assessing the behaviour of the lower crust. Lithospheric geodynamic  
490 models should evaluate the effect of mineral mode variations beyond simplistic predictions  
491 for highly efficient metamorphism, and evaluate its influence on lithospheric dynamics. A  
492 metastable and thus mechanically strong lower crust has been considered to control  
493 exhumation dynamics and topographic expression in thickened crustal sequences (e.g.  
494 Jackson et al., 2004). In Fiordland, incomplete metamorphism in the Breaksea Orthogneiss  
495 plausibly maintained positive buoyancy in lower crust that might otherwise have been  
496 capable of foundering (Chapman et al., 2017).

497

## CONCLUSIONS

498 A novel method utilising mineral orientation relationships, lattice strain and mineral  
499 chemistry collected via large-scale EBSD and EDS/WDS analysis can be used to quantify the  
500 proportion of metastable igneous minerals within a patchily deformed high-grade  
501 orthogneiss. Detailed mapping of microstructural and physiochemical relations indicates that  
502 up to 32% of the Breaksea Orthogneiss mineralogy is igneous, the remainder being  
503 metamorphic. The heterogeneous nature of the deformation facilitated the preservation of  
504 igneous mineralogy in intermediate protoliths, best developed in strain shadows to more  
505 competent material such as eclogite. The greater intensity of strain in less competent portions  
506 of the orthogneiss assisted metamorphic transformation. Metamorphic transformation at the  
507 grain scale was coincident with dynamic recrystallization, consistent with a causal role for  
508 strain in assisting reaction progress in water-poor rocks. The method highlights how  
509 inefficient metamorphism can be, even at the high-grade conditions commonly considered  
510 amenable to complete crustal transformation.

511

## ACKNOWLEDGMENTS

512 TC was supported by an Australian Postgraduate Award from the University of Sydney.  
513 Logistical and analytical funding was provided by the School of Geosciences, the University  
514 of Sydney (GLC) and through the ARC Discovery Project and Future Fellowship  
515 (DP120102060 to SP and NRD; FT1101100070 to SP). D. Cyprych and P. Trimby are  
516 thanked for help with data collection, and the Department of Conservation in Te Anau for  
517 permission to visit and sample localities at Breaksea Sound, Fiordland National Park. The  
518 authors acknowledge the facilities, scientific and technical assistance of the Australian  
519 Microscopy & Microanalysis Research Facility at the Australian Centre for Microscopy &  
520 Microanalysis at the University of Sydney. The manuscript was improved after reviews from  
521 A. Indares and editorial handling of P. Cordier. This is contribution XX from the ARC Centre

522 of Excellence for Core to Crust Fluid Systems (<http://www.CCFS.mq.edu.au>) and XX from  
523 GEMOC (<http://www.GEMOC.mq.edu.au>). The analytical data were obtained using  
524 instrumentation funded by DEST Systemic Infrastructure Grants, ARC LIEF, NCRIS,  
525 industry partners and Macquarie University.

526

#### REFERENCES CITED

- 527 Allibone, A.H., Jongens, R., Turnbull, I.M., Milan, L.A., Daczko, N.R., De Paoli, M.C., &  
528 Tulloch, A.J. (2009a). Plutonic rocks of western Fiordland, New Zealand: field  
529 relations, geochemistry, correlation and nomenclature. *New Zealand Journal of*  
530 *Geology and Geophysics*, 52, 379–415.
- 531 Austrheim, H., Erambert, M., & Engvik, A.K. (1997). Processing of crust in the root of the  
532 Caledonian continental collision zone: the role of eclogitization. *Tectonophysics*, 273,  
533 129–153.
- 534 Betka, P.M., & Klepeis, K.A. (2013). Three-stage evolution of lower crustal gneiss domes at  
535 Breaksea Entrance, Fiordland, New Zealand. *Tectonics*, 32, 1084–1106.
- 536 Bradshaw, J.Y. (1989). Origin and metamorphic history of an Early Cretaceous polybaric  
537 granulite terrain, Fiordland, southwest New Zealand. *Contributions to Mineralogy and*  
538 *Petrology*, 103, 346–360.
- 539 Bunge, H.J. (1982). *Texture analysis in materials science*. Butterworths, London.
- 540 Bürgmann, R., & Dresen, G. (2008). Rheology of the lower crust and upper mantle: evidence  
541 from rock mechanics, geodesy, and field observations. *Annual Reviews of Earth and*  
542 *Planetary Sciences*, 36, 531–567.
- 543 Brenker, F.E., Prior, D.J., & Müller, W.F. (2002). Cation ordering in omphacite and effect on  
544 deformation mechanism and lattice preferred orientation (LPO). *Journal of Structural*  
545 *Geology*, 24, 1991–2005.
- 546 Chapman, T., Clarke, G.L., Daczko, N.R., Piazzolo, S., & Rajkumar, A. (2015).

- 547 Orthopyroxene–omphacite- and garnet–omphacite-bearing magmatic assemblages,  
548 Breaksea Orthogneiss, New Zealand: oxidation state controlled by high-*P* oxide  
549 fractionation. *Lithos*, 216–217, 1–16.
- 550 Chapman, T., Clarke, G.L., & Daczko, N.R. (2016). Crustal differentiation in a thickened arc  
551 — evaluating depth dependencies. *Journal of Petrology*, 57, 595–620.
- 552 Chapman, T., Clarke, G.L., Piazzolo, S., & Daczko, N.R. (2017). Evaluating the importance of  
553 metamorphism in the foundering of continental crust. *Scientific Reports* 7,  
554 DOI:10.1038/s41598-017-13221-6.
- 555 Clarke, G.L., Daczko, N.R., & Miescher, D. (2013). Identifying relict igneous garnet and  
556 clinopyroxene in eclogite and granulite, Breaksea Orthogneiss, New Zealand. *Journal*  
557 *of Petrology*, 54, 1921–1938.
- 558 Cyprych, D., Piazzolo, S., & Almqvist, B.S.G. (2017). Seismic anisotropy from compositional  
559 banding in granulites from the deep magmatic arc of Fiordland, New Zealand. *Earth*  
560 *and Planetary Science Letters*, 477, 156–167.
- 561 Daczko, N.R., & Halpin, J.A. (2009). Evidence for melt migration enhancing recrystallization  
562 of metastable assemblages in mafic lower crust, Fiordland, New Zealand. *Journal of*  
563 *Metamorphic Geology*, 27, 167–185.
- 564 De Paoli, M.C., Clarke, G.L., Klepeis, K.A., Allibone, A.H., & Turnbull, I.M. (2009). The  
565 eclogite–granulite transition: mafic and intermediate assemblages at Breaksea Sound,  
566 New Zealand. *Journal of Petrology*, 50, 2307–2343.
- 567 De Paoli, M.C., Clarke, G.L., & Daczko, N.R. (2012). Mineral equilibria modeling of the  
568 granulite–eclogite transition: effects of whole-rock composition on metamorphic  
569 facies type-assemblages. *Journal of Petrology*, 53, 949–970.

- 570 Droop, G.T.R. (1987). A general equation for estimating Fe<sup>3+</sup> concentrations in  
571 ferromagnesian silicates and oxides from microprobe analyses, using stoichiometric  
572 criteria. *Mineralogical Magazine*, 51, 431–435.
- 573 Flinn, D. (1965). On the symmetry principle and the deformation ellipsoid. *Geological*  
574 *Magazine*, 102, 36–45.
- 575 Green, D.H., & Ringwood, A.E. (1967). An experimental investigation of the gabbro to  
576 eclogite transformation and its petrological applications. *Geochimica et*  
577 *Cosmochimica Acta*, 31, 767–833.
- 578 Holness, M.B. (2006). Melt-solid dihedral angles of common minerals in natural rocks.  
579 *Journal of Petrology*, 47, 791–800.
- 580 Holness, M.B., Vukmanovic, Z., & Mariani, E. (2017). Assessing the role of compaction in  
581 the formation of adcumulates: a microstructural perspective. *Journal of Petrology*, 58,  
582 643–674.
- 583 Holness, M.B., Clemens, J.D. & Vernon, R. H. (2018). How deceptive are microstructures in  
584 granitic rocks? Answers from integrated physical theory, phase equilibrium, and  
585 direct observations. *Contributions to Mineralogy and Petrology*, 173, 2–18.
- 586 Jackson, J.A., Austrheim, H., McKenzie, D., & Priestley, K. (2004). Metastability,  
587 mechanical strength, and the support of mountain belts. *Geology*, 32, 625–628.
- 588 Jamtveit, B., Austrheim, H., & Malthe-Sørensen, A. (2000). Accelerated hydration of the  
589 Earth's deep crust induced by stress perturbations. *Nature*, 408, 75–78.
- 590 Klepeis, K.A., King, D., De Paoli, M., Clarke, G.L. & Gehrels, G. (2007). Interaction of  
591 strong lower and weak middle crust during lithospheric extension in western New  
592 Zealand. *Tectonics*, 26, 1–27.



- 593 Klepeis, K.A., Schwartz, J., Stowell, H., & Tulloch, A.J. (2016). Gneiss domes, vertical and  
594 horizontal mass transfer, and the initiation of extension in the hot lower-crustal root of  
595 a continental arc, Fiordland, New Zealand. *Lithosphere*, 8, 116–140.
- 596 Kruse, R., Stünitz, H., & Kunze, K. (2001). Dynamic recrystallization processes in  
597 plagioclase porphyroclasts. *Journal of Structural Geology*, 23, 1111–1115.
- 598 Marmo, B.A., Clarke, G.L., & Powell, R. (2002). Fractionation of bulk rock composition due  
599 to porphyroblast growth: effects of eclogite facies mineral equilibria, Pam Peninsula,  
600 New Caledonia. *Journal of Metamorphic Geology*, 20, 151–165.
- 601 Mainprice, D., Hielscher, R., & Schaeben, H. (2011). Calculating anisotropic physical  
602 properties from texture data using the MTEX open-source package. In Prior, D. J.,  
603 Rutter, E. H., Tatham, D. J. (Eds.) *Deformation mechanisms, rheology and tectonics:  
604 microstructures, mechanics and anisotropy*. Geological Society of London Special  
605 Publication 360, 175–192.
- 606 Milan, L.A., Daczko, N.R., Clarke, G.L., & Allibone, A.H. (2016). Complexity of *in situ* U  
607 Pb–Hf isotope systematics during arc magma genesis at the roots of a Cretaceous arc,  
608 Fiordland, New Zealand. *Lithos*, 264, 296–314.
- 609 Milan, L.A., Daczko, N.R. & Clarke, G.L. (2017). Cordillera Zealandia: A Mesozoic arc  
610 flare-up on the palaeo-Pacific Gondwana margin. *Scientific Reports*,  
611 doi:10.1038/s41598-017-00347-w.
- 612 Miranda, E.A., & Klepeis, K.A. (2016). The interplay and effects of deformation and  
613 crystallized melt on the rheology of the lower continental crust, Fiordland, New  
614 Zealand. *Journal of Structural Geology*, 93, 91–105.
- 615 Morimoto, N. (1989). Nomenclature of pyroxenes. *Canadian Mineralogist*, 27, 143–156.

- 616 Paterson, S.R., Vernon, R.H., & Tobisch, O.T. (1989). A review of criteria for the  
617 identification of magmatic and tectonic foliations in granitoids. *Journal of Structural*  
618 *Geology*, 11, 349–363.
- 619 Piazzolo, S., Bestmann, M., Prior, D.J., & Spiers, C.J. (2006). Temperature dependent grain  
620 boundary migration in deformed-then-annealed material: observations from  
621 experimentally deformed synthetic rocksalt. *Tectonophysics*, 427, 55–71.
- 622 Piazzolo, S., La Fontaine, A., Trimby, P., Harley, S., Yang, L., Armstrong, R., & Cairney, J.  
623 (2016). Deformation-induced trace element redistribution in zircon revealed using  
624 atom probe tomography. *Nature Communications*, DOI: 10.1038/ncomms10490.
- 625 Powell, R. Guiraud, M., & White, R.W. (2005). Truth and beauty in metamorphic phase  
626 equilibria: conjugate variables and phase diagrams. *The Canadian Mineralogist*, 43,  
627 21–33.
- 628 Prior, D.J., Boyle, A.P., Brenker, F., Cheadle, M.C., Day, A., Lopez, G., Peruzzo, L., Potts,  
629 G.J., Reddy, S., Spiess, R., Timms, N.E., Trimby, P., Wheeler, J., & Zetterström, L.  
630 (1999). The application of electron backscatter diffraction and orientation contrast  
631 imaging in the SEM to textural problems in rocks. *American Mineralogist*, 84, 1741–  
632 1759.
- 633 Prior, D.J., Wheeler, J., Peruzzo, L., Spiess, R., & Storey, C. (2002). Some garnet  
634 microstructures: an illustration of the potential of orientation maps and misorientation  
635 analysis in microstructural studies. *Journal of Structural Geology*, 24, 999–1011.
- 636 Racek, M., Štípská, P., & Powell, R. (2008). Garnet–clinopyroxene intermediate granulites in  
637 the St. Leonhard massif of the Bohemian Massif: ultrahigh-temperature  
638 metamorphism at high pressure or not? *Journal of Metamorphic Geology*, 26, 253–  
639 271.

- 640 Satsukawa, T., Piazzolo, S., González-Jiménez, J.M., Colás, V., Griffin, W.L., O'Reilly, S.Y.,  
641 Gervilla, F., Fanlo, I., & Kerestedjian, T.N. (2015). Fluid-present deformation aids  
642 chemical modification of chromite: insights from chromites from Golyamo  
643 Kamenyane, SE Bulgaria. *Lithos*, 228–229, 78–89.
- 644 Smith, J.R., Piazzolo, S., Daczko, N.R., & Evans, L. (2015). The effect of pre-tectonic  
645 reaction and annealing extent on behaviour during subsequent deformation: Insights  
646 from paired shear zones in the lower crust of Fiordland, New Zealand. *Journal of*  
647 *Metamorphic Geology*, 33, 557–577.
- 648 Štípská, P., & Powell, R. (2005). Does ternary feldspar constrain the metamorphic conditions  
649 of high-grade meta-igneous rocks? Evidence from orthopyroxene granulites,  
650 Bohemian Massif. *Journal of Metamorphic Geology*, 23, 627–647.
- 651 Stowell, H.H., Schwartz, J.J., Klepeis, K.A., Hout, C., Tulloch, A.J., & Koenig, A. (2017).  
652 Sm-Nd garnet ages for granulite and eclogite in the Breaksea Orthogneiss and  
653 widespread granulite facies metamorphism of the lower crust, Fiordland magmatic  
654 arc, New Zealand. *Lithosphere*, DOI: 10.1130/L662.1.
- 655 Stünitz, H. (1998). Syndeformational recrystallization — dynamic or compositionally  
656 induced? *Contributions to Mineralogy and Petrology*, 131, 219–236.
- 657 Stüwe, K. (1997). Effective bulk composition changes due to cooling: a model predicting  
658 complexities in retrograde reaction textures. *Contributions to Mineralogy and*  
659 *Petrology*, 129, 43–52.
- 660 Svahnberg, H., & Piazzolo, S., 2010. The initiation of strain localization in plagioclase-rich  
661 rocks: insights from detailed microstructural analyses. *Journal of Structural Geology*,  
662 32, 1404–1416.

- 663 Urai, J.L., Means, W.D., & Lister, G.S. (1986). Dynamic recrystallization of minerals. In  
664 Hobbs, B.E., Heard, H.C. (Eds.). Mineral and rock deformation (laboratory studies).  
665 Geophysical monograph of the American Geophysical Union, 36, pp. 161–200.
- 666 White, R.W., & Clarke, G.L. (1997). The role of deformation in aiding recrystallization: an  
667 example from a high-pressure shear zone, Central Australia. *Journal of Petrology*, 38,  
668 1307–1329.
- 669 Williams, M.L., Dumond, G., Mahan, K., Regan, S., & Holland, M. (2014). Garnet-forming  
670 reactions in felsic orthogneiss: implications for densification and strengthening the  
671 lower crust. *Earth and Planetary Science Letters*, 405, 207–219.
- 672 Vernon, R.H. (2004). *A practical guide to rock microstructure*. Cambridge University Press,  
673 Cambridge, UK.
- 674 Vernon, R.H., White, R.W., & Clarke, G.L. (2008). False metamorphic events inferred from  
675 misinterpretation of microstructural evidence and  $P$ – $T$  data. *Journal of Metamorphic*  
676 *Geology*, 26, 437–449.
- 677 Vernon, R.H. & Paterson, S.R. (2008). How extensive are subsolidus grain-shape changes in  
678 cooling granites? *Lithos*, 105, 42–50.
- 679 Vernon, R.H., Collins, W.J., & Cook, N.D.J. (2012). Metamorphism and deformation of  
680 mafic and felsic rocks in a magma transfer zone, Stewart Island, New Zealand.  
681 *Journal of Metamorphic Geology*, 30, 473–488.
- 682 Yund, R.A., & Tullis, J. (1991). Compositional changes of minerals associated with dynamic  
683 recrystallization. *Contributions to Mineralogy and Petrology*, 108, 346–355.

684 **Figure captions**

685 **Figure 1a** Simplified geological map of the Breaksea Sound area between northern  
686 Resolution Island and Coal River. Circles show sample locations and inset shows the  
687 structure at Breaksea Tops. Structural relationships in red and foliation trajectories are from

688 Klepeis et al. (2016). **b** Detailed outcrop relationships showing distribution of strain  
689 surrounding an eclogite pod, near sample location 0904D.

690 **Figure 2a** Hand specimens of the monzogabbroic to monzodioritic gneiss showing typical  
691 variation in mineral assemblages and strain. Boxes represent approximate locations of studied  
692 samples, MG = monzogabbroic and MD = monzodioritic. **b** Flinn diagram of mafic cluster  
693 shapes. Values of  $D$  represent the intensity of strain defined as the distance from the origin,  
694 and  $K$  the slope defines the type of strain symmetry.

695 **Figure 3a** Mafic grain cluster in low-strain monzogabbroic gneiss comprising intergrown  
696 igneous garnet and omphacite (see Fig. 6). Omphacite grains in places have coincidental  
697 crystal form. **b** Deformed omphacite phenocryst with faceted and euhedral plagioclase  
698 inclusions (arrow). **c** Large Igneous garnet with crystallographically aligned rutile exsolution  
699 (arrow) and faceted plagioclase inclusion displaying a perfect growth twin (arrow). **d** Large  
700 interlocking plagioclase grains in low-strain monzogabbroic gneiss. Note the low apparent  
701 dihedral angles, undulose extinction, sutured grain boundaries (arrows) and small neoblasts. **e**  
702 Large omphacite porphyroclasts in intermediate-strain monzodioritic gneiss, with internal  
703 titano-hematite exsolution. **f** Variably recrystallised feldspar-rich matrix in an intermediately-  
704 strained monzogabbroic gneiss. Large plagioclase porphyroclasts are present in the top right,  
705 neoblasts occur closer to the cluster margins. **g** Attenuated mafic grain clusters in high-strain  
706 monzodioritic gneiss, surrounded by necklaces of neoblastic garnet, quartz, rutile and K-  
707 feldspar. **h** Granoblastic feldspar-rich matrix from high-strain monzodioritic gneiss. Grain  
708 triple junctions are close to  $120^\circ$  (arrow).

709 **Figure 4** Lower hemisphere pole figures displaying omphacite CPO (one point per grain) for  
710 the studied strain gradients.  $J$  = texture index, MUD refers to maximum mean uniform  
711 distribution values,  $n$  is the number of grains and  $AR$  ( $X/Y$ ) is the mean aspect ratio of grain

712 cluster from the samples. Int. = intermediate. Top to the right sense of shear. Maps  
713 accompanying the pole figures are shown in Figure 9.

714 **Figure 5** Lower hemisphere pole figures displaying plagioclase (one point per grain) CPO for  
715 the studied strain gradients.  $J$  = texture index, max refers to mean uniform distribution values  
716 and  $n$  is the number of grains. Maps accompanying the pole figures are shown in Figure 9.

717 **Figure 6** Microstructures from two samples of monzogabbroic gneiss. **a** EBSD mineral map  
718 of grain cluster in low-strain monzogabbroic gneiss (0904D: Fig. 3a), low angle (2–10°)  
719 subgrain boundaries (sgb) shown in yellow and grain boundaries (>10°: gb) in black. Black  
720 arrows point to small neoblasts and white arrows to porphyroclasts. **b** Crystal misorientation  
721 profile showing gradual lattice distortion in porphyroclast marked in **a**. **c** Misorientation axis  
722 distribution (crystal coordinate reference frame) across a low-angle boundary (2–10°) in  
723 garnet shown in **a**. **d** Lower hemisphere pole figures utilising the XYZ structural reference  
724 frame (one point per grain) of omphacite grains in the cluster shown in **a**. MUD refers to the  
725 maximum mean uniform distribution and  $n$  is the number of grains. **e** Orientation contrast  
726 forescatter image of omphacite grain cluster in the intermediate-strain monzogabbroic gneiss  
727 (0905B). **f–g** Crystallographic misorientation from specific reference point (red cross) in  
728 porphyroclast (rainbow; **f**) and neoblast (green; **g**). **h** Lower hemisphere pole figures of  
729 omphacite grains across the microstructure (shown by circle and squares in **e**). Rotation from  
730 porphyroclast orientations to those of grains in the tails is apparent. **i–j** Crystal misorientation  
731 profiles showing gradual lattice distortion in porphyroclast (**f**) and neoblast (**g**).

732 **Figure 7** Crystallographic misorientation from specific reference point (red cross: **a**) and  
733 associated profile (white line) showing lattice distortion and subgrain orientation and mineral  
734 jadeite content in omphacite fish from the intermediate-strain monzodioritic gneiss (**b**).

735 **Figure 8** Microstructures from two samples of monzodioritic gneiss. **a** Backscatter electron  
736 image of grain cluster in intermediate strain monzodioritic gneiss (1203T: Fig. 3e). **b–e**

737 Crystallographic misorientation from specific reference point (red cross) and associated  
738 profiles showing gradual lattice distortion and subgrain orientation in omphacite  
739 porphyroclast (rainbow; **b & d**) and neoblast (green; **c & e**). **f** Misorientation axis distribution  
740 (crystal coordinate reference frame) across a low-angle boundary ( $2\text{--}10^\circ$ ) shown in **b**. **g**  
741 Backscatter electron image of omphacite grain cluster in high-strain monzodioritic gneiss  
742 (1203C: Fig. 3g). **h–k** Crystallographic misorientation from specific reference point (red  
743 cross) and associated profiles showing gradual lattice distortion and subgrain orientation in  
744 omphacite porphyroclast (rainbow; **h & j**) and neoblast (green; **i & k**). **l** Pole figures of  
745 adjacent omphacite and garnet grains (red & black dots in **a**).

746 **Figure 9** Composite ternary plot of feldspar, garnet and clinopyroxene microprobe analyses,  
747 respectively with apices Ab–Or–An, Jd–Aeg–Q and Pyp–Alm–Grs+Sps for strain  
748 proportions of monzogabbro (MG) and monzodiorite (MD) in the Breaksea Orthogneiss.

749 **Figure 10** Schematic of the microstructural and chemical distinctions across microstructures.  
750 Chemical variation diagram of plagioclase anorthite content (An), garnet grossular content  
751 (Grs) and omphacite jadeite (Jd) content across the profile, arrows represent within sample  
752 variability that changes across igneous and neoblasts (arrow head), subordinate to overall  
753 changes across the strain gradient. Simple pole figure displays igneous omphacite CPO.

754 **Figure 11** Large-scale EBSD maps of (**a–b**) low- and intermediate-strain monzogabbroic and  
755 (**c–d**) intermediate- and high-strain monzodioritic gneisses. Highlighted grains represent  
756 material interpreted as igneous relicts based on location, grain size and internal deformation,  
757 transparent grains are neoblasts.

758 **Supplementary Figure 1** Lower hemisphere pole figures displaying clinopyroxene CPO  
759 (one point per grain) for cumulate clinopyroxenite and eclogite in the Breaksea Orthogneiss.  
760 MUD refers to maximum mean uniform distribution values and  $n$  is the number of grains.

761 **Supplementary Figure 2** WDS X-ray maps from intermediate-strain monzodioritic gneiss  
762 (0905B) **a** phase map with grain boundaries in black and subgrain boundaries in yellow of Al  
763 **(b)**, Ca **(c)** and Na **(d)** proportions in omphacite, Ca **(e)** and Mg **(f)** proportions in garnet and  
764 Ca proportions in plagioclase **(g)**. Zoning in omphacite overprints all grains. Garnet zoning is  
765 asymmetrical towards mineral boundaries with plagioclase. Plagioclase albite content is  
766 zoned towards omphacite. Image size is *c.* 2 x 2 cm.

767

768

769

770

771

772

773

774

775

776

777

778

779

780

781

782

783

784

785



786  
787  
788  
789  
790  
791  
792  
793  
794  
795  
796  
797  
798  
799  
800  
801  
802  
803  
804  
805  
806

**Table 1** Summary of the tectonometamorphic history of the Breaksea Orthogneiss.

<i>T</i> (Ma)	<i>P</i> (GPa)	<i>T</i> (°C)	<i>D</i>	assemblages	tectonometamorphic event	ref.
124– 115	1.8	950– 1200	Ign	Grt–Omp– Pl–Opx	Pluton emplacement, layering and accumulation	1, 2, 3, 4, 8
124– 115	1.8	800– 950	D <sub>1</sub>	Grt–Omp– Pl	Metamorphism and S <sub>1</sub> –L <sub>1</sub> fabric	1, 2, 5, 6, 8
115– 105	10–1.4	650– 750	Post-D <sub>1</sub>	Di–Ab and Hb–Pl	Near-isothermal decompression, decimetre dome formation	1, 5, 6
105– 90	0.9–1.4	650– 750	D <sub>2</sub>	Hb–Pl	Extensional shear zones, collapse and foundering	1, 6, 7, 8

1 Chapman et al. (2017); 2 Clarke et al. (2013); 3 Chapman et al. (2015); 4 Milan et al. (2016); 5 De Paoli et al. (2009); 6 Klepeis et al. 2016); 7 Klepeis et al. (2007); 8 Stowell et al. (2017)

807

808

**Table 2** Observed mineral modes across the two strain profiles and predicted modes from mineral equilibria modelling of a monzodiorite and monzogabbro at  $T = 850^{\circ}\text{C}$  and  $P = 1.8 \text{ GPa}$  after Chapman et al. (2017).

	monzogabbro			monzodiorite		
	low-strain 0904D	intermediate -strain 0905B	modelled	intermediate -strain 1203T	high-strain 1203C	modelled
grt <sub>lg</sub>	24	16		3		
grt <sub>N</sub>		4	28		24	25
omp	25	21	32	24	24	29
pl	45	49	22	60	31	27
kfs	0.5	3.5	0.5	10	9	2
ky	1	2	6	0.5	3	3
rt	1	2	1	1	1	1
qtz	1.5	0.5	3.5	1	6	6
ap	0.5	1	na	0.5	1	na
hbl	1.5	1			1	
mu			5*			7*

\*models overestimate mu on account of small proportions of H<sub>2</sub>O, partially reducing kfs mode

809

810

811

812

813

814

815

816

817



**Table 3** Representative electron microprobe analysis of minerals from the two strain profiles.

low-strain MG 0904D	omp <sub>Ig</sub> core	omp <sub>Ig</sub> rim	grt <sub>Ig</sub> core	grt <sub>Ig</sub> rim	pl <sub>Ig</sub>	pl <sub>N</sub>
SiO <sub>2</sub>	51.69	52.25	39.44	39.46	63.08	63.98
TiO <sub>2</sub>	0.54	0.49	0.06	0.06	0.00	0.00
Al <sub>2</sub> O <sub>3</sub>	11.27	11.47	21.34	21.23	22.74	22.57
Cr <sub>2</sub> O <sub>3</sub>	0.00	0.00	0.00	0.00	0.00	0.00
FeO	7.51	7.14	21.33	21.30	0.08	0.06
MnO	0.00	0.00	0.49	0.53	0.00	0.00
MgO	8.43	8.10	11.21	11.23	0.00	0.00
CaO	16.14	15.40	6.47	6.66	3.87	3.86
Na <sub>2</sub> O	4.91	5.40	0.05	0.04	9.30	9.47
K <sub>2</sub> O	0.00	0.00	0.00	0.00	0.66	0.43
Total	100.49	100.25	100.39	100.51	99.73	100.37

**Table 3** cont.

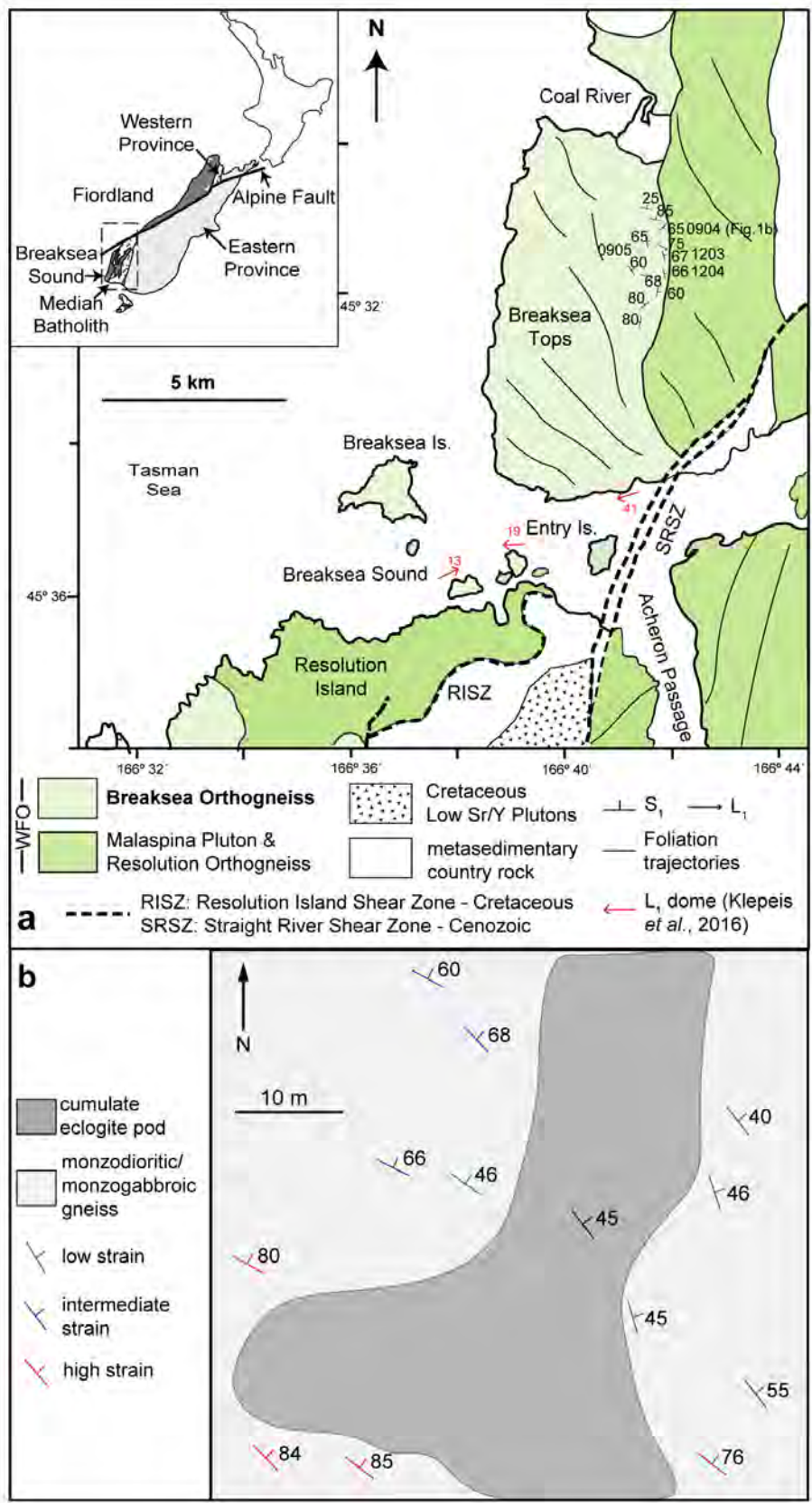
int.-strain MG 0905B	omp <sub>Ig</sub>	omp <sub>N</sub>	grt <sub>Ig</sub> core	grt <sub>Ig</sub> rim	pl <sub>Ig</sub>	pl <sub>N</sub>
SiO <sub>2</sub>	49.92	61.07	38.79	38.83	62.28	61.76
TiO <sub>2</sub>	1.00	0.00	0.08	0.07	0.00	0.00
Al <sub>2</sub> O <sub>3</sub>	9.42	24.38	21.84	21.71	23.52	23.74
Cr <sub>2</sub> O <sub>3</sub>	0.00	0.00	0.00	0.00	0.00	0.00
FeO	8.65	0.34	21.27	20.56	0.10	0.09
MnO	0.06	0.00	0.54	0.41	0.00	0.00
MgO	9.22	0.07	9.91	9.16	0.00	0.00
CaO	18.21	6.40	7.91	9.40	5.20	5.24
Na <sub>2</sub> O	3.50	7.80	0.04	0.03	8.42	8.35
K <sub>2</sub> O	0.00	0.34	0.00	0.00	0.49	0.70
Total	99.98	100.40	100.46	100.17	100.01	99.88

**Table 3** cont.

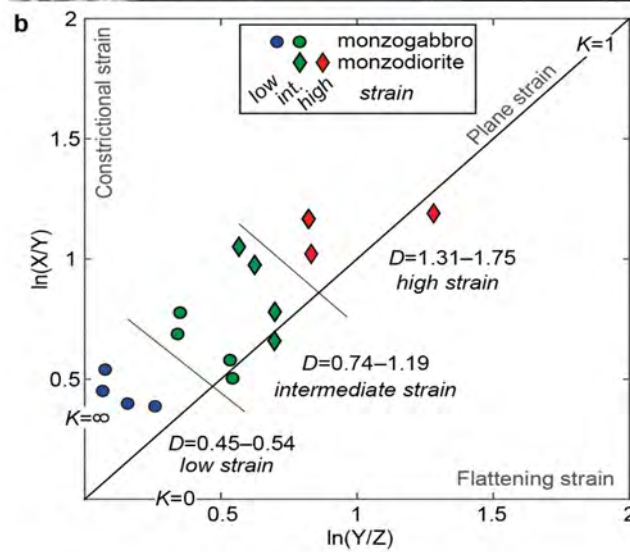
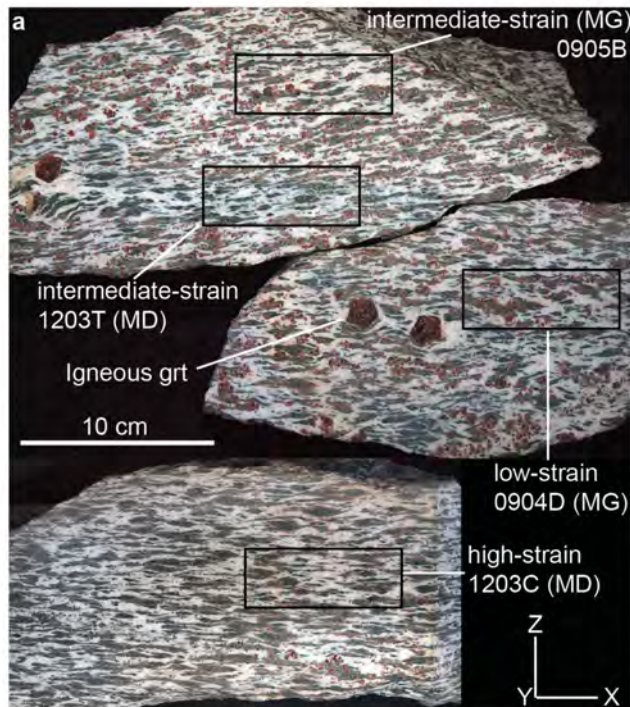
Int.-strain MD 1203T	omp <sub>Ig</sub>	omp <sub>N</sub>	grt <sub>Ig</sub> core	grt <sub>Ig</sub> rim	pl <sub>Ig</sub>	pl <sub>N</sub>
SiO <sub>2</sub>	51.19	49.99	39.35	39.65	61.00	61.42
TiO <sub>2</sub>	0.32	0.58	0.04	0.09	0.00	0.00
Al <sub>2</sub> O <sub>3</sub>	6.07	13.06	22.11	22.20	23.82	24.04
Cr <sub>2</sub> O <sub>3</sub>	0.01	0.00	-0.01	0.02	0.00	0.00
FeO	8.56	8.61	21.38	21.87	0.07	0.05
MnO	0.06	0.05	0.66	0.63	0.00	0.00
MgO	11.36	7.32	9.83	10.17	0.00	0.00
CaO	19.90	15.49	7.38	6.29	4.89	4.98
Na <sub>2</sub> O	2.35	4.94	0.03	0.01	8.56	8.43
K <sub>2</sub> O	0.00	0.01	0.01	0.00	0.52	0.50
Total	100.08	100.28	100.92	101.03	98.95	99.49

**Table 3** cont.

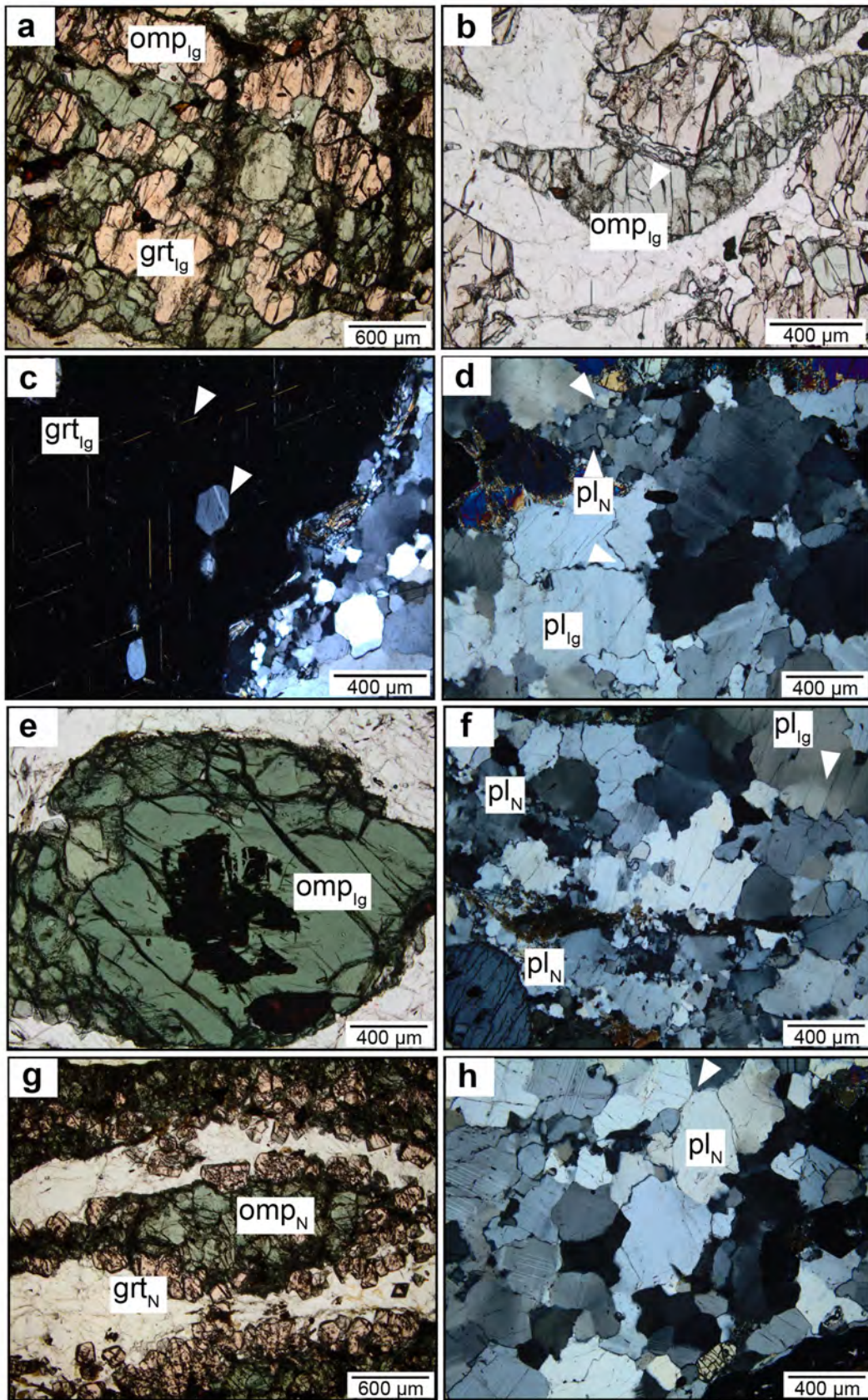
high-strain MD 1203C	omp <sub>N</sub> core	omp <sub>N</sub> rim	grt <sub>N</sub> core	grt <sub>N</sub> rim	pl <sub>RN</sub> core	pl <sub>N</sub> rim
SiO <sub>2</sub>	50.95	52.04	38.74	38.77	62.02	62.45
TiO <sub>2</sub>	0.74	0.63	0.05	0.03	0.00	0.00
Al <sub>2</sub> O <sub>3</sub>	10.28	10.04	21.78	21.96	23.34	23.38
Cr <sub>2</sub> O <sub>3</sub>	0.05	0.00	0.00	0.00	0.00	0.00
FeO	8.26	8.00	21.70	21.19	0.00	0.00
MnO	0.04	0.00	0.57	0.45	0.00	0.00
MgO	8.46	8.51	10.11	9.51	0.00	0.00
CaO	16.67	16.36	6.83	8.24	5.06	5.02
Na <sub>2</sub> O	4.27	4.55	0.02	0.00	8.60	8.89
K <sub>2</sub> O	0.00	0.00	0.00	0.00	0.48	0.47
Total	99.72	100.13	99.80	100.15	99.50	100.21



Chapman et al. Figure 1

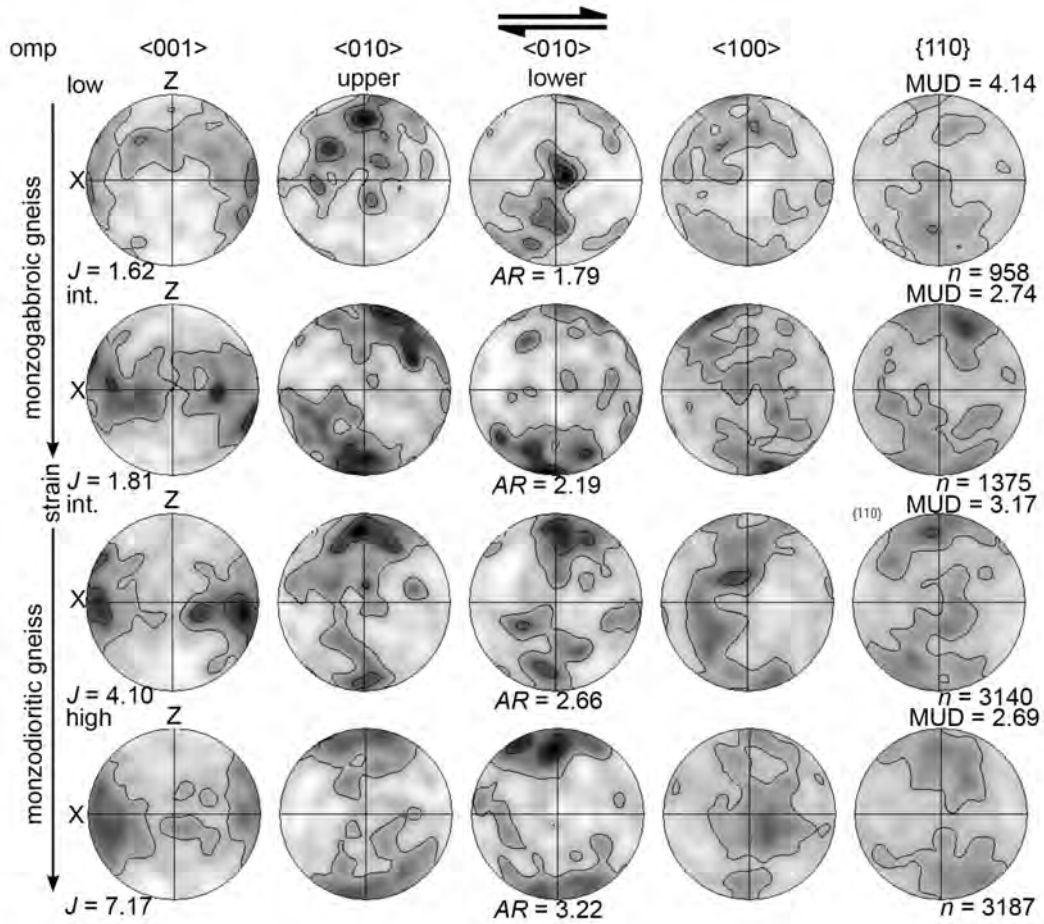


Chapman et al. Figure 2

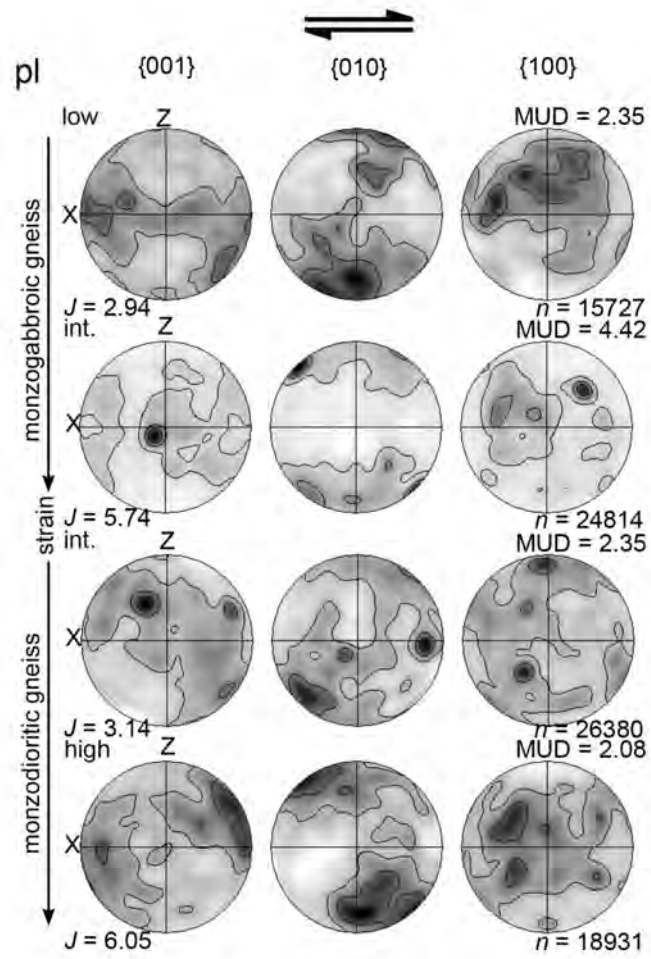


Chapman et al. Figure 3

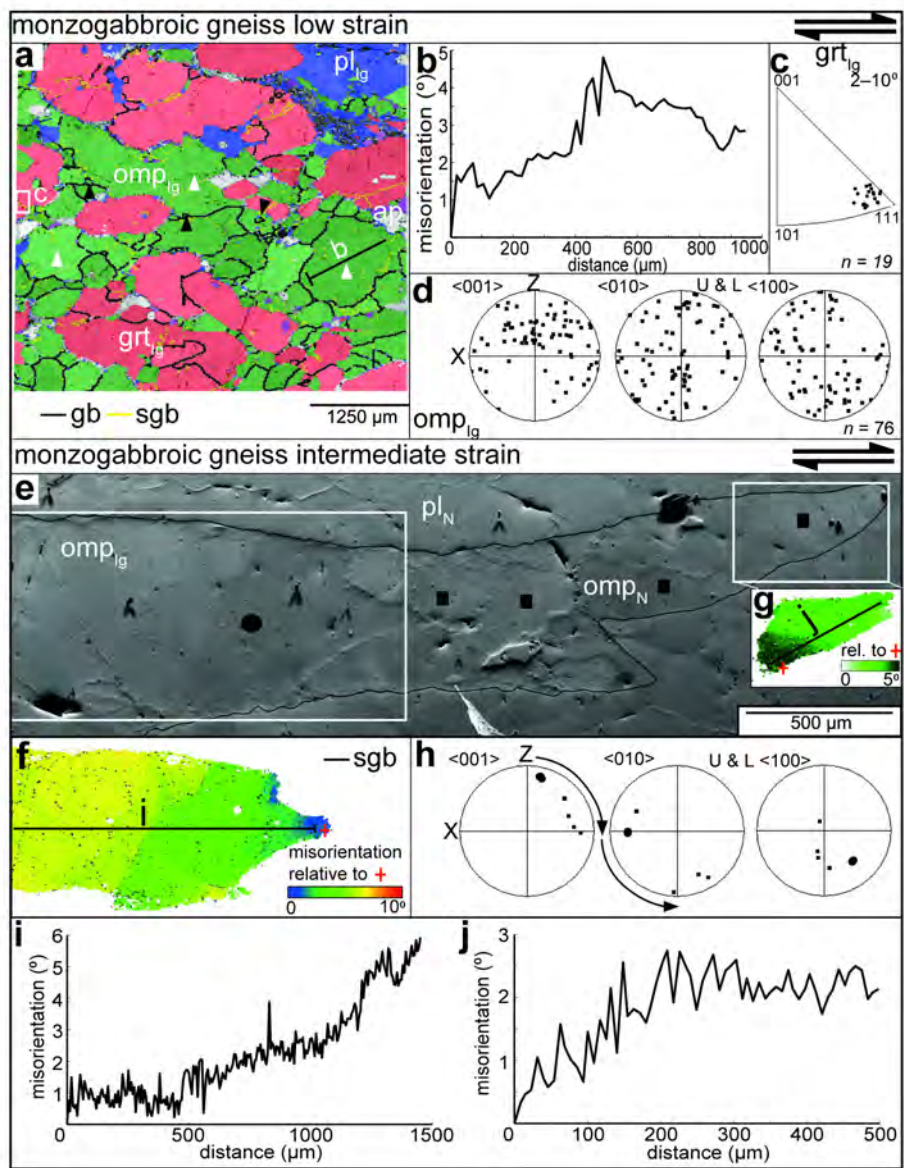




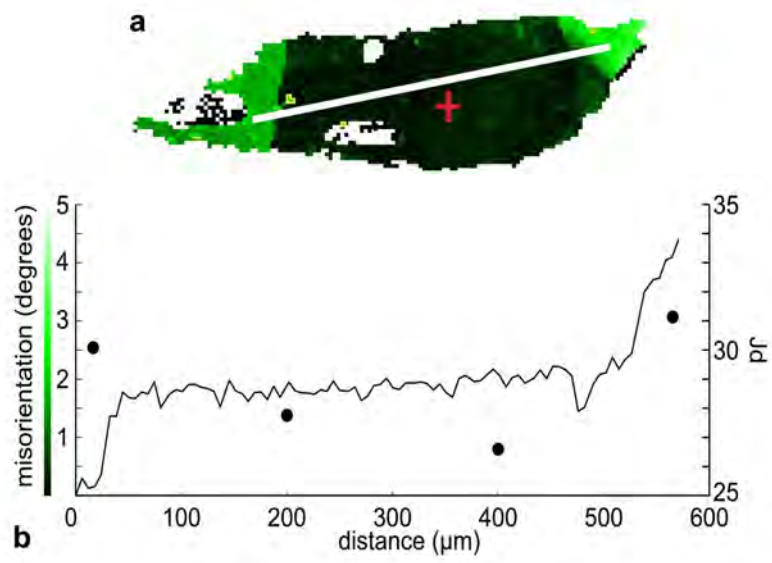
Chapman et al. Figure 4



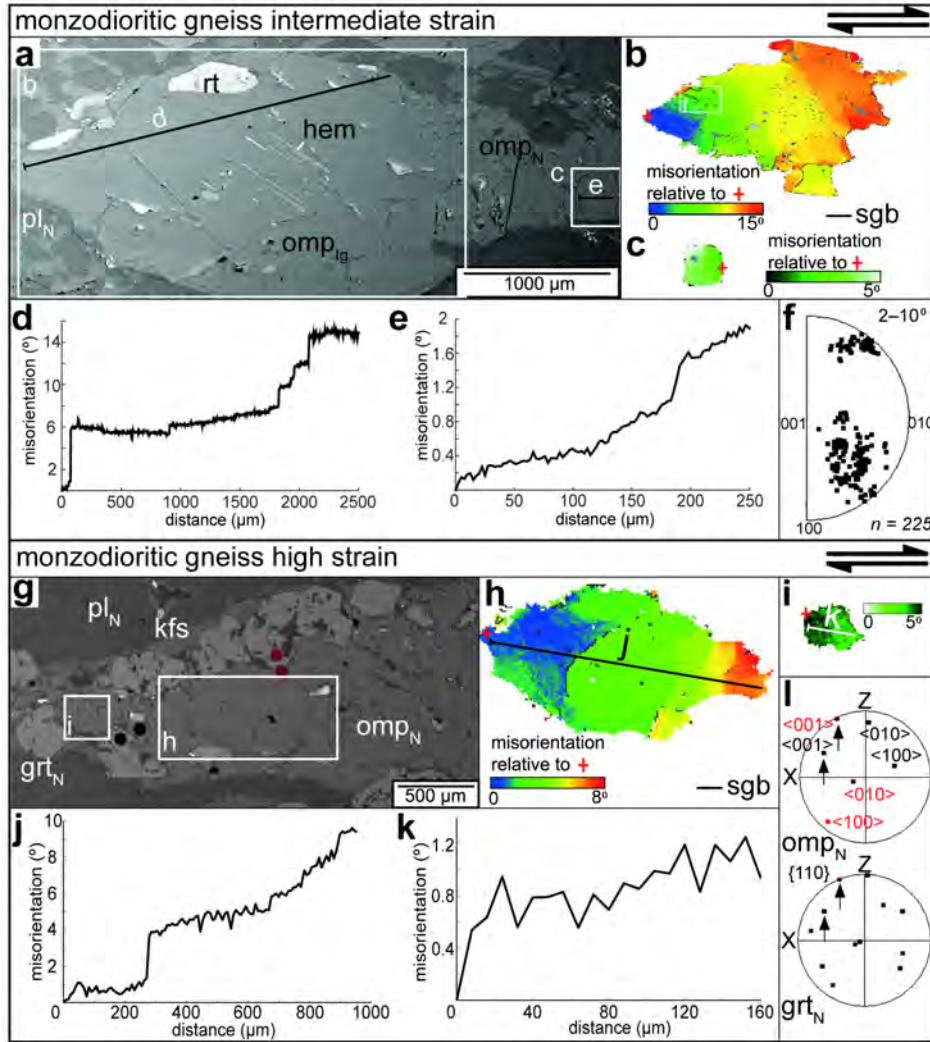
Chapman et al. Figure 5



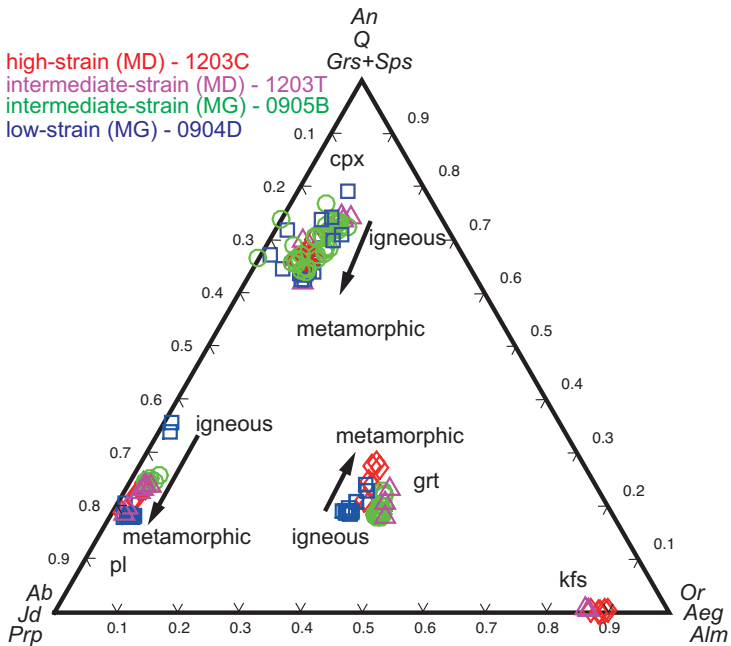
Chapman et al. Figure 6



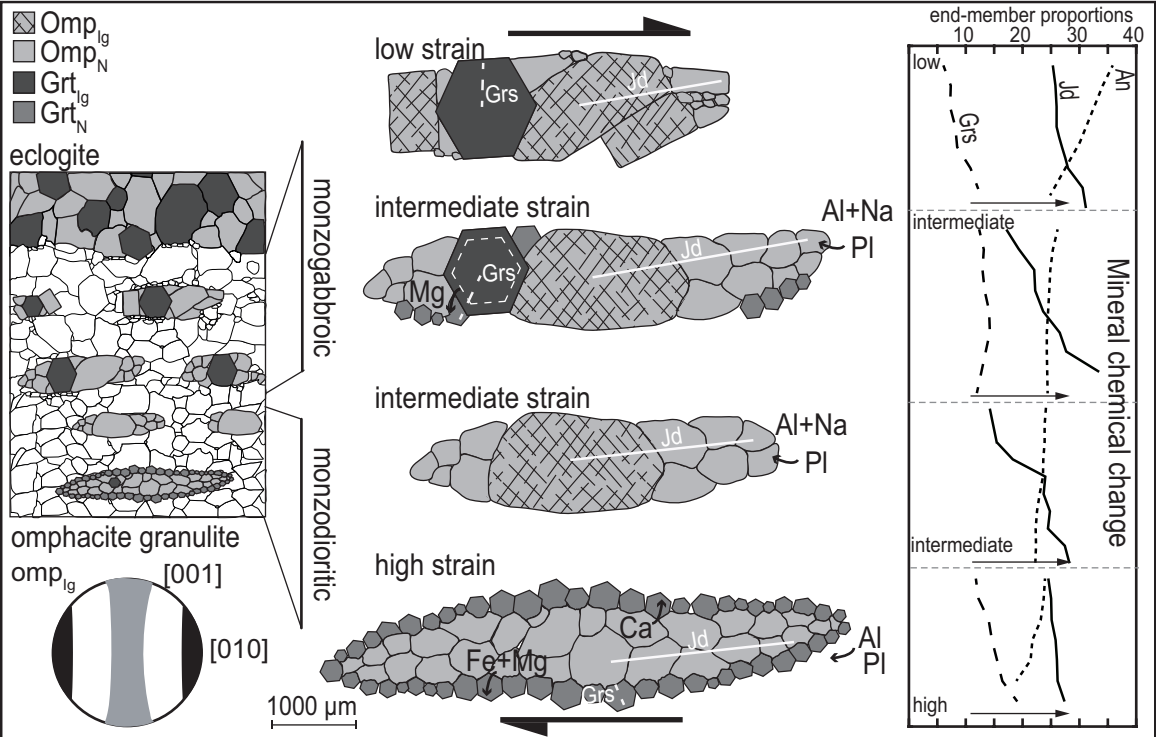
Chapman et al. Figure 7



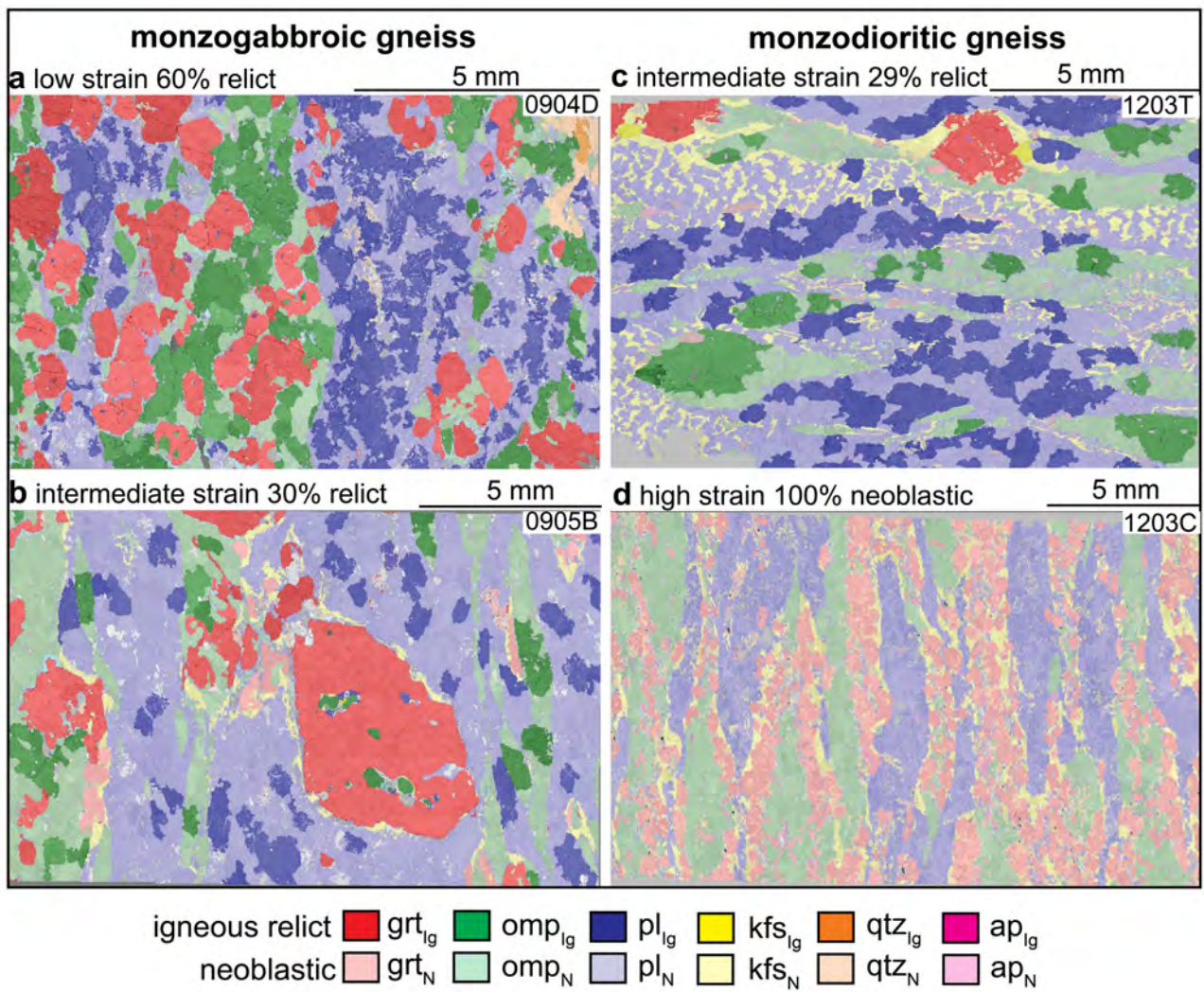
Chapman et al. Figure 8



Chapman et al. Figure 9



Chapman et al. Figure 10



Chapman et al. Figure 11